



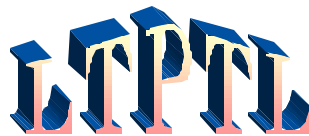
Low Temperature Plasma Technology Laboratory

Design and Performance of Distributed Helicon Sources

Francis F. Chen, John D. Evans, and George R. Tynan

LTP-008

August, 2000



Electrical Engineering Department
Los Angeles, California 90095-1594

Design and performance of distributed helicon sources

Francis F. Chen*, John D. Evans*, and George R. Tynan†

*University of California, Los Angeles, California 90095-1594

†University of California, San Diego; La Jolla, California 92093-0417

ABSTRACT

Helicon plasma sources are known to be efficient generators of high-density plasma for materials processing applications. By using multiple sources, arbitrarily large substrates can in principle be covered uniformly with dense plasma. To test this idea, a seven-tube helicon source was constructed, and the plasma density and uniformity measured. Densities up to 10^{12} cm⁻³ over a 40-cm diameter area with $\pm 3\%$ uniformity were achieved.

I. INTRODUCTION

Because of their ability to produce high-density plasma efficiently, helicon sources have been intensely studied^{1,2} in recent years, particularly in connection with materials processing. Helicon sources differ from other inductively coupled radiofrequency (RF) plasmas (ICPs) in that a DC magnetic field \mathbf{B}_0 is required. Once the gas in the processing chamber has been weakly ionized by the electrostatic voltages on the antenna, the presence of \mathbf{B}_0 allows the antenna to launch circularly polarized waves, called helicon waves, into the plasma; and the energy of these waves is subsequently converted to electron energy, thus raising the electron temperature T_e and causing rapid ionization to occur. Since helicon waves are weakly damped in the plasma, the mechanism of this conversion process is complicated and has been in dispute. Our present understanding is that the helicon waves transfer their energy to the plasma particles not directly but through the excitation of another wave at the boundary. This secondary wave, a type of electron cyclotron wave, is called a Trivelpiece-Gould (TG) mode, and it is this wave which is readily absorbed by the plasma.

Commercial helicon reactors capable of etching 200-cm diam wafers have been produced^{3, 4} and used⁵ successfully. A prototype source for 300-mm wafers has been constructed by one of the authors (GT) and shown to give uniform coverage. For larger substrates, a single source becomes problematical because the energy deposition by TG modes is computed⁶ to be localized near the radial boundary, and this would lead to a density depression near the axis. For this reason, we have investigated the possibility of covering large substrates with a number of small helicon sources spaced appropriately. To prove that this is possible requires answering the following questions: 1) What type of small source is most suitable; 2) How can the RF power be divided equally to the individual sources; and 3) Can the plasma from each source be merged to produce uniform coverage of a large area? These questions will be answered in turn.

II. DESIGN OF INDIVIDUAL SOURCES

Type 1 helicon sources. Numerous experiments, confirmed by theory, have shown that the right-hand circularly polarized ($m = +1$) azimuthal mode of the helicon wave produces the highest downstream density at a given power. Our Type 1 source (Fig. 1), there-

fore, is driven by a half-wavelength helical antenna, which preferentially excites this mode⁷. The quartz or glass tube is 5 cm in diam and is surrounded by a plastic coil form on which 400 turns of 28 AWG coated magnet wire is wound to form a solenoid capable of producing dc magnetic fields up to 100 G. The 10 cm long antenna is made of 1 cm wide copper sheet and is fed from a matching network through a BNC connector. This design was based on the simplest helicon dispersion relation, which can be written in mks units as⁸

$$k_{\perp} \approx \frac{3.83}{a} = e\mu_0 \left(\frac{\omega}{k_{\parallel}} \right) \left(\frac{n}{B_0} \right), \quad (1)$$

where n is the plasma density, $\omega = 2\pi f$ the rf angular frequency, a the tube radius, and 3.83 the first zero of the J_1 Bessel function. A half-wavelength antenna of length L preferentially excites k_{\parallel} values near π/L . For $a = 2.5$ cm and $f = 27.12$ MHz, Eq. (1) can be written in practical units as

$$n_{11} \approx 1.4B_G / L_{\text{cm}}, \quad (2)$$

where n_{11} is in units of 10^{11} cm^{-3} , and B_G is the magnetic field in gauss. Thus, the 10-cm antenna is resonant with a plasma density of $\approx 7 \times 10^{11} \text{ cm}^{-3}$ at $B_0 = 50$ G. This value of n is a reasonable target for the source when densities of order 10^{11} cm^{-3} are desired at the substrate level. In any case, the optimum n varies with ω and B_0 over a reasonable range.

The value of B_0 was chosen to take advantage of a low-field density peak which has been observed in tubes of 4-5 cm diameter⁸. Though Eq. (1) predicts that n will decrease with B_0 , this relation fails below 100 G, and a local peak in density is usually seen around 30-50 G. We believe that this peak is due to an eigenmode of the combined helicon-TG wave; but whatever its cause, it offers reasonably high density at economically low magnetic fields. Extensive measurements of the plasma injected into a processing chamber by this source have been reported earlier⁹. For instance, the radial density profile 6 cm below the flange on which the source is located is shown in Fig. 2 for $f = 27.12$ MHz, $B_0 = 50$ G, and various rf powers P_{rf} . These profiles indicate the coverage provided by each individual source. The width of the profile does not depend sensitively on B_0 , since the field downstream is too weak to confine the plasma. Figure 3 shows the peak density for this case vs B_0 . The density is seen to decrease more or less monotonically with B_0 , in disagreement with Eq. (1), and no peak occurs in the neighborhood of 50 G, as would be expected. This reason for this behavior, as explained in Ref. 9, is that the field from the small, closely coupled solenoid diverges so rapidly that more and more plasma is diverted into the sides of the flange aperture as B_0 is increased. The magnetic field lines in the single-tube experimental chamber with a Type 1 source are shown in Fig. 4. Also shown are electron Larmor orbits at various positions for 100 G in the source. These Larmor diameters vary from small to large relative to the scalelength of ∇B_0 , making numerical modeling of the source very difficult.

In spite of the difficulty with the small solenoids, the discharge inside the tube is bright blue, and the density is in the 10^{12} cm^{-3} range, indicating that the discharge is a helicon discharge and not an unmagnetized ICP. Furthermore, the discharge is much weaker when B_0 is reversed to excite the $m = -1$ mode, showing the directionality typical of $m = 1$ helicon discharges.

Type 1A helicon sources. An obvious solution to the scrape-off problem is to replace the small solenoids with a large coil of diameter comparable to that of the main chamber. A diagram of this source, called Type 1A, can be found in Ref. 9, and the coil used will be

shown in Sec. V. With this change of field coil, the low-field density peak is easily found, as seen in Fig. 5, which compares the densities with the two magnetic configurations. Fig. 6 shows n vs B_0 for both directions of \mathbf{B}_0 (corresponding to launching $m = +1$ and -1 waves downwards). For this source, both modes give comparable densities on axis, but the $m = +1$ mode produces more plasma in a wider profile, as seen in Fig. 7, and thus provides much better area coverage. Helical antennas of different lengths and with more turns, covering 1 and 2 wavelengths, were also tested in this experiment, as well as on another helicon device, but the half-wavelength antenna shown in Fig. 1 performed the best.

Type 2 helicon sources. At this point it was found experimentally that an $m = 0$ antenna — that is, an axisymmetric loop — was almost as efficient as an $m = 1$ helical antenna in producing plasma, a finding later confirmed by computations with the HELIC code.¹⁰ A Type 2 source (Fig. 8) was designed, differing from Type 1A in three primary respects. First, the antenna consists of a single loop of wire, which is much more compact than a helical antenna. This loop may be divided into N turns for best coupling to the rf matching network. Such an antenna is obviously non-directional, and in order to prevent propagation of energy away from the chamber, the insulating glass, quartz, or ceramic “tube” is reduced to a short belljar, greatly reducing the height of the source. Finally, an insulating annulus, or “skirt”, is added to the belljar to reduce the eddy currents induced in the metal flange by the antenna. Figure 9 compares the densities achieved with the Type 1A and Type 2 sources as the direction of \mathbf{B}_0 is reversed. It is clear that the helical antenna is sensitive to the sign of \mathbf{B}_0 , but the $m = 0$ antenna is not. When the inductance of the $m = 0$ antenna is optimized, both antennas give comparable densities below ≈ 100 G. Figure 10 shows that the straighter field lines of a large coil give better results than a tightly fitting small solenoid in a Type 2 source, as was the case for Type 1. As the number of turns N in the $m = 0$ loop antenna is increased, the efficiency of the antenna changes depending on the external circuitry; the optimum is $N \approx 3-5$. This variation is illustrated in Fig. 11. Fig. 12 shows the effect of adding an insulating skirt to minimize eddy currents induced by the antenna. RF powers of 135 W and 1.1 kW are shown; note that the benefit of the skirt disappears at high power.

Conventional $m = 0$ helicon sources, such as the MØRI[®] source³, use two loops with current in opposite directions, spaced a half-wavelength apart ($L = \lambda/2$). However, we find that the single-loop Type 2 source can create more plasma than a MØRI source. A comparison is shown in Fig. 13. Type 2 sources also appear to have particularly good downstream properties which can lead to large-area coverage. Fig. 14 shows density profiles at two axial positions, $z = 3$ and 10 cm, and at two RF powers, $P_{\text{rf}} = 135$ W and 1 kW. The diffusion of plasma as it streams away from the source is apparent; however, at the higher power there is more plasma (evaluated by integrating the curves of Fig. 14 over the entire cross section) at $z = 10$ cm than at $z = 3$ cm. This effect could be caused by downstream ionization, but it is not known why it is not observed with other sources.

III. DESIGN OF DISTRIBUTED SOURCES

To avoid confusion, an individual source will henceforth be called a “tube”, including its antenna and its individual field coil and gas feed, if any. Power figures refer to total power to the array. The first multi-tube source consisted of seven Type 1 tubes, with one in the center and six surrounding it, as shown in Fig. 15. The source (Fig. 16) is placed on top of a processing chamber which has an array of permanent magnets on its circumference to provide confinement of primary electrons: a “magnetic bucket.”

RF power can be distributed to all the tubes from a single power supply. We have considered three ways to divide the power. First, the tubes can be connected in series. This would be necessary for plasma arcs, which have a negative resistance, so that one tube does not take all the power. Since they have a positive resistance, this is not necessary for helicon sources; and, in fact, a series connection has too high an impedance for a match to be obtained with reasonable values of capacitances in a conventional matching network. Second, one can consider each tube to be one element of a lumped transmission line. Finally, one can simply connect the tubes in parallel, and this method turned out to be the best. The electrical circuit is shown in Fig. 17. The matching network is conventional, with two variable vacuum capacitors. The power is fed to seven cables of equal length connecting to the individual tubes. The length of the cables must be carefully considered in setting the capacitors.

IV. EXPERIMENTS WITH TYPE 1 TUBES

Figures 18 and 19 show density profiles vs B_0 and P_{rf} in argon and chlorine discharges with a Type 1 array, taken with the probe shown in Fig. 15, which reaches nearly to the center of the array. Because of slower diffusion in Cl, the structure of the individual tubes manifests itself in the observed radial density profiles. In Fig. 19(b), the central tube failed to ignite at 2 kW. Better uniformity was observed even for Cl at $z = 27$ cm; this is shown in Fig. 20. Because small solenoids were used, these initial experiments produced plasma densities only in the 10^{10} cm⁻³ range and were discontinued in favor of Type 1A and Type 2 tubes. Nonetheless, breakdown and sustainment of bright discharges in all seven tubes was achieved. The well known jump transition to the helicon wave mode is shown in Fig. 21 for Cl. The breakdown and sustaining powers for A and Cl are shown in Fig. 22 as functions of pressure for $B_0 = 0$. Note that once breakdown has occurred in all seven tubes, the discharge can be sustained with only ≈ 25 W total power. Finally, the low-field peak and the directionality of the helical Type 1A antennas are shown for an array source in Fig. 23.

V. EXPERIMENTS WITH TYPE 2 TUBES

For the major part of this work, an array of seven Type 2 tubes was used, encircled by a large magnetic field coil, as shown in Fig. 24. The tubes were arranged as in Fig. 15, but the diameter of the array was increased to accommodate the larger Type 2 sources with insulating skirts. Two experimental chambers with surface-field confinement were available, shown in Fig. 25, and the source could be placed on top of either chamber. Since the bolt-circle-diameter of the array was designed for the smaller chamber, density profiles taken in the large chamber show a falloff near the edge which can easily be eliminated by adjusting the spacing of the tubes. Also shown in Fig. 24 is a ‘‘Lazy Susan’’ probe, consisting of eight ion collectors arranged along a radius of an aluminum plate. The plate can be moved vertically and can be rotated to measure azimuthal symmetry of the plasma. Fig. 26 shows the design of an individual ion collector.

With a Type 2 array, densities in the 10^{11-12} cm⁻³ range were readily achieved. The insensitivity of the $m = 0$ antenna to the direction of \mathbf{B}_0 is shown in Fig. 27. Note that a Type 2 array, with only the central tube energized, produces much higher density than a 7-tube array of Type 1A tubes at the same power. The existence of the low-field density peak in a Type 2 source is shown in Fig. 28. This peak appears for P_{rf} above 50 W and maximizes for $P_{rf} = 200$ W. As P_{rf} is raised to >300 W, the density keeps rising and does not fall at high fields. The downstream plasma conditions are shown in Fig. 29 for Cl. The density is uniform but falls off radially for the reason given above. The electron temperature is constant at ≈ 2 eV, and the plasma potential V_p is nearly constant at ≈ 8 V.

Density profiles near the source are given in Fig. 30 for argon and Fig. 31 for chlorine as functions of (a) B_0 and (b) P_{rf} . Note that densities approaching $2 \times 10^{12} \text{ cm}^{-3}$ over a 30-cm diameter are achieved in argon. Ignition in chlorine is more difficult, and in this run apparently some of the tubes did not fire. Fig. 32 shows more uniform density profiles 27 cm downstream, where the density is still of order 10^{12} cm^{-3} in argon.

To prove the principle of distributed sources, it is important to show that the plasma from the individual tubes diffuses fast enough to give a uniform density profile within a reasonable distance of the source. For this reason, the Lazy Susan probe was developed to measure the azimuthal symmetry of the ion flux at wafer level. Saturation ion currents were measured on the radial array of collectors as the plate was rotated to various angles θ , and the currents were converted to densities using the Bohm formula. An example of the raw data is shown in Fig. 33. It is clear that the collectors have different sensitivities, and in order to calibrate them, radial Langmuir probe scans were made near the collectors. An example of such a scan is shown in Fig. 34. The density 3.5 cm above the collector plate appears to be extremely uniform except near the wall, where the multidipole field of the wall magnets affects the discharge. At 0.5 cm above the plate, there appear to be irregularities due to the collectors themselves. In any case, the deviation from uniformity is much smaller than Fig. 33 would suggest, and the average of the two curves on Fig. 34 was used to calibrate the Lazy Susan probe. An example of an azimuthal density scan in the large chamber is shown in Fig. 35. Significant deviation from azimuthal uniformity can be seen in the outermost curve. Fig. 36 is a polar plot of a scan in the small chamber, with n plotted radially in absolute units. Deviations from uniformity can be seen for $r > 11$ cm. These data were taken at low density; at higher density, diffusion would improve the uniformity. The density near the wall is shown in Fig. 37. The structure of the permanent magnet array of the magnetic bucket can be seen, as well as an $m = 1$ asymmetry due to the gas feed. Note, however, that there is no noticeable $m = 6$ asymmetry due to the individual tubes. The density variations are seen more clearly in the 3D surface plot in Fig. 38, and in the density contour plot in Fig. 39. Uniformity of $\pm 3\%$ is maintained over most of a 30-cm diameter surface; no $m = 6$ asymmetry is seen; and the ripples due to the magnetic bucket can be seen only near the edge.

The uniformity can in principle be improved by using separate power supplies for each tube. To test this, we used two independent RF sources at 27.12 MHz, driving 3 and 4 of the tubes, respectively, the azimuthal symmetry in Fig. 35 is improved to that shown in Fig. 40. The structure of the asymmetries is more easily seen in the contour plot of Fig. 41. Again, there is uniformity to $\pm 3\%$ over a most of the area, and there are no indications of an $m = 6$ perturbation arising from the deployment of the individual tubes.

VI. CONCLUSIONS

A compact large-area plasma source based on helicon discharges has been designed and tested. Uniform plasmas of density up to 10^{12} cm^{-3} have been produced with multiple sources in a distributed array. After the completion our work at PMT, Inc., a similar experiment was published by Heinrich et al.¹¹ with four ICP sources in a rectangular array. The present experiment, with 7 helicon sources in a circular array, has produced both higher density and better uniformity. Thus, we have demonstrated in principle the feasibility of covering large substrates with high-density plasma. This method can be developed into a plasma processing tool for semiconductor wafers >300 mm in diameter and for flat-panel displays of arbitrary size, as well as for other ultra-large-area plasma processing applications.

VII. ACKNOWLEDGMENTS

This work was supported by PMT, Inc. (now Trikon, Inc.), the Semiconductor Research Corporation, and the National Science Foundation.

FIGURE CAPTIONS

- Fig. 1. Schematic of a Type 1 helicon source.
- Fig. 2. Radial density profiles with Type 1 source at $f = 27.12$ MHz, $B_0 = 50$ G, $p_0 = 18$ mTorr of argon, and various rf powers P_{rf} , taken at $z = 6$ cm below the mounting flange and at various radii r from the axis. These definitions of f , B_0 , p_0 , P_{rf} , z , and r will be used in succeeding figure captions, and the gas will be argon unless otherwise noted.
- Fig. 3. Peak density vs. B_0 at various powers in a Type 1 source. 18 mTorr, 27.12 MHz, $z = 6$ cm, $r = 0$.
- Fig. 4. Schematic of Type 1 test chamber showing magnetic field lines and outlines of the plasma tube, solenoid, entrance flange, and experimental chamber. Probe scans were made at the positions of the arrows. The ellipses show the electron Larmor orbit sizes at various positions when the field in the source is 100 G.
- Fig. 5. Comparison of Type 1 and Type 1A sources. 10 mTorr A, 720 W, 13.46 MHz.
- Fig. 6. Low-field density peak with the Type 1A source. 10 mTorr, 1.25 kW, 13.56 MHz, $z = 3$ cm, $r = 5$ cm.
- Fig. 7. Density profiles of Type 1A source at $r = 0$ for the $m = +1$ and -1 helicon modes. 150 G, 1 kW, 15 mTorr, 13.56 MHz, $z = 3$ cm.
- Fig. 8. Schematic of a Type 2 source.
- Fig. 9. Density on axis vs magnetic field with $m = \pm 1$ and single-turn $m = 0$ antennas for both directions of B_0 . 435 W, 10 mTorr, 13.56 MHz.
- Fig. 10. Density on axis vs B_0 with an $m = 0$ antenna and two types of field coil. The tube length was 7 cm in both cases. 10 mTorr, 720 W, 13.56 MHz, $N = 3$.
- Fig. 11. Dependence of density on the number of turns N in the $m = 0$ antenna. 15 mTorr, 120 G, 13.56 MHz, $z = 3$ cm, $r = 0$.
- Fig. 12. Effect of an insulating skirt in a Type 2 source at $P_{\text{rf}} = 135$ and 1100 W. 10 mTorr, 13.56 MHz, $N = 3$, $z = 3$ cm, $r = 0$.
- Fig. 13. Density produced by a Type 2 source with $N = 3$, compared with that from a MØRI source with $L = 5$ cm ($\lambda = 10$ cm). 15 mTorr, 120 G, 13.56 MHz, $z = 2$ cm, $r = 0$.
- Fig. 14. Density profiles illustrating the diffusion of plasma between $z = 3$ and 10 cm. 20 mTorr, 80 G, 13.56 MHz, $r = 0$.
- Fig. 15. Arrangement of tubes in a 7-tube distributed source.
- Fig. 16. Schematic of a 7-tube source with a magnetic bucket. The Type 1 tubes are arranged as in Fig. 15 (not in line, as depicted here).
- Fig. 17. Schematic of the matching and distribution circuit.

- Fig. 18. Density profiles along one radius of a 7-tube array of Type 1 sources vs (a) magnetic field at $P_{\text{rf}} = 1.75$ kW, and (b) RF power at $B_0 = 30$ G. 18 mTorr A, 13.56 MHz, $z = 9$ cm.
- Fig. 19. Density profiles along one radius of a 7-tube array of Type 1 sources vs (a) magnetic field at $P_{\text{rf}} = 3$ kW, and (b) RF power at $B_0 = 30$ G. 10 mTorr Cl, 13.56 MHz, $z = 9$ cm.
- Fig. 20. Diffusion of plasma in a Type 1 array source between $z = 9$ and 27 cm. 10 mTorr Cl, 2.5 kW, 13.56 MHz, 30 G.
- Fig. 21. Jump transition in a Type 1 array as P_{rf} is increased. 10 mTorr Cl, 30 G, 13.56 MHz, $r = 0$.
- Fig. 22. RF power required to break down and sustain A and Cl discharges in a Type 1 array, as a function of p_0 at $B_0 = 0$
- Fig. 23. The low-field density peak in a Type 1 array source appearing strongly when the direction of B_0 corresponds to the excitation of the $m = +1$ helicon mode. 4 mTorr Cl, 3.3 kW, $z = 20$ cm, $r = 5$ cm.
- Fig. 24. Schematic of a Type 2 array source with large magnet coil. Also shown is the “Lazy Susan” rotatable ion collector array.
- Fig. 25. Experimental setup with magnet buckets of two diameters.
- Fig. 26. Schematic of an ion collector in the rotatable probe array.
- Fig. 27. Density vs B_0 in $m = 0$ array sources, showing insensitivity to field direction. Top: a single Type 2 tube with $N = 1$, $z = 10$ cm, $r = 5$ cm. Bottom: a 7-tube Type 1A array with $N = 5$.
- Fig. 28. The low-field density peak at intermediate powers in a Type 2 array. 8 mTorr, 13.56 MHz, $N = 5$.
- Fig. 29. Radial profiles of n , T_e , and V_p in a Type 2 source. R is the radial distance from the wall. V_p is given on the right-hand scale. 3 mTorr Cl, 35 G, 3 kW, 13.56 MHz, $z = 27$ cm.
- Fig. 30. Radial density profiles in argon in a Type 2 source, as functions of (a) B_0 and (b) P_{rf} . 5 mT, 20 G, 2 kW, 13.56 MHz, $N = 2$, $z = 7$ cm unless otherwise noted.
- Fig. 31. Radial density profiles in chlorine in a Type 2 source, as functions of (a) B_0 and (b) P_{rf} . 3 mT, 20 G, 2 kW, 13.56 MHz, $N = 2$, $z = 7$ cm unless otherwise noted.
- Fig. 32. Downstream radial density profiles in (a) 5 mTorr A at 20 G and (b) 3 mTorr Cl at 35 G in a Type 2 source. $f = 13.56$ MHz, $N = 2$, $z = 27$ cm.
- Fig. 33. Raw data from the Lazy Susan probe. 3 mTorr Cl, 20 G, 2 kW, 13.56 MHz, $N = 2$, $z = 30$ cm.
- Fig. 34. Radial density profile with Langmuir probe at $z = 27.5$ cm and Lazy Susan probe at $z = 28$ and 31 cm. 2 mTorr, 60 G, 1.4 kW, 13.56 MHz, $N = 4$.
- Fig. 35. Azimuthal density uniformity at various radii in a 20×20 cm cross section at $z = 30$ cm. The density at each radius is plotted relative to the dashed circle at that radius. 2 mTorr A, 40 G, 1.4 kW, $N = 4$.
- Fig. 36. Polar plots of $n(\theta)$ with increasing radius in units of 10^{11} cm^{-3} . 20 mTorr A, 75 G, 1.3 kW, 13.56 MHz, $z = 20$ cm.

- Fig. 37. Azimuthal density scan at $r = 15$ cm, about 1.5 cm from permanent magnet array on wall.
- Fig. 38. 3D plot of the data of Fig. 36.
- Fig. 39. Density contour plot of the data of Fig. 36. The contour interval is $\approx 4\%$. Only the data inside the 40-cm diameter circle is meaningful.
- Fig. 40. Polar plot of density at various radii (cm) with two independently adjustable power supplies. 15 mTorr A, 100 G, 1.6 kW, 27.12 MHz, $N = 2$.
- Fig. 41. Contour plot of the data of Fig. 40. The contour interval is 3%. Only the data inside the 40-cm diameter circle is meaningful.

REFERENCES

- ¹ R.W. Boswell and F.F. Chen, IEEE Trans. Plasma Sci. **25**, 1229 (1997).
- ² F.F. Chen and R.W. Boswell, IEEE Trans. Plasma Sci. **25**, 1245 (1997).
- ³ G.A. Campbell, D.I.C. Pearson, and A.P. deChambrier, Proc. 33rd Annual Techn. Conf., Society of Vacuum Coaters (1990).
- ⁴ B. Chapman, N. Benjamin, C.F.A. van Os, R.W. Boswell, and A.J. Perry, 12th Symposium on Dry Process, Denki-Gakkai, Tokyo (1991).
- ⁵ G.R. Tynan, A.D. Bailey III, G.A. Campbell, R. Charatan, A. de Chambrier, G. Gibson, D.J. Hemker, K. Jones, A. Kuthi, C. Lee, T. Shoji, and M. Wilcoxson, J. Vac. Sci. Technol. A **15**, 2885 (1997).
- ⁶ D. Arnush and F.F. Chen, Phys. Plasmas **5**, 1239 (1998).
- ⁷ D.G. Miljak and F.F. Chen, Plasma Sources Sci. Technol. **7**, 61 (1998).
- ⁸ F.F. Chen, J. Vac. Sci. Technol. A **10**, 1389 (1992).
- ⁹ F. F. Chen, X. Jiang, and J.D. Evans, J. Vac. Sci. Technol. A **18**, xxxx (2000).
- ¹⁰ D. Arnush, Phys. Plasmas **7**, 3042 (2000).
- ¹¹ F. Heinrich, U. Bänziger, A. Jentzsch, G. Neumann, and C. Huth, J. Vac. Sci. Technol. B **14**, 2000 (1996).

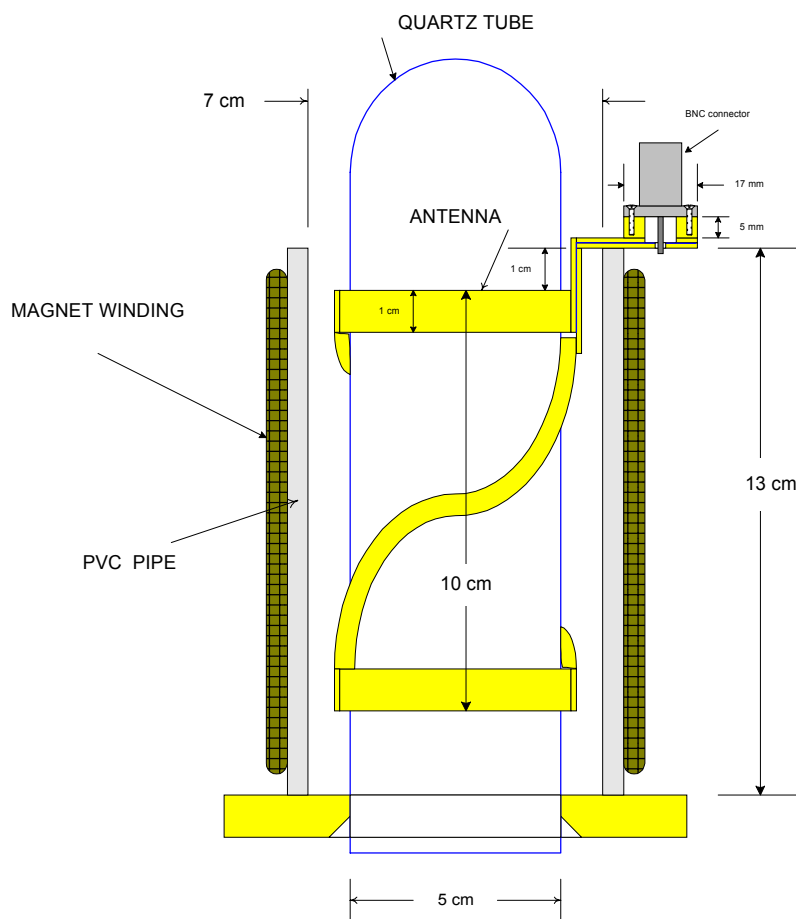


Fig. 1. Schematic of a Type 1 helicon source.

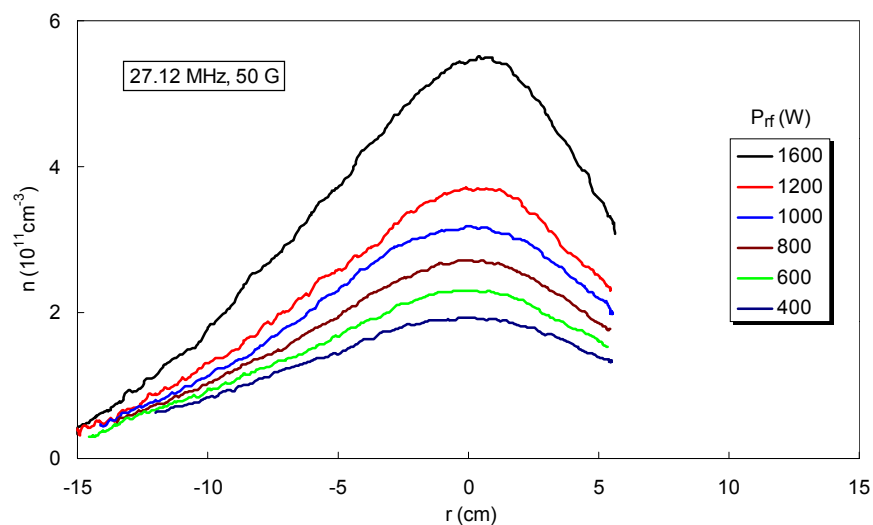


Fig. 2. Radial density profiles with Type 1 source at $f = 27.12$ MHz, $B_0 = 50$ G, $p_0 = 18$ mTorr of argon, and various rf powers P_{rf} , taken at $z = 6$ cm below the mounting flange and at various radii r from the axis. These definitions of f , B_0 , p_0 , P_{rf} , z , and r will be used in succeeding figure captions, and the gas will be argon unless otherwise noted.

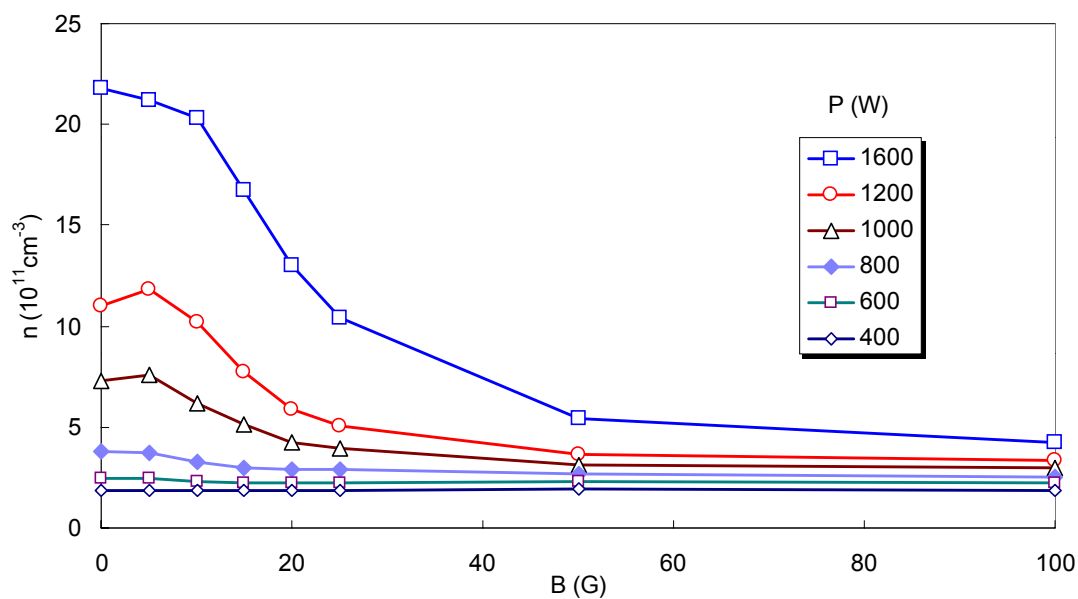


Fig. 3. Peak density vs. B_0 at various powers in a Type 1 source. 18 mTorr, 27.12 MHz, $z = 6$ cm, $r = 0$.

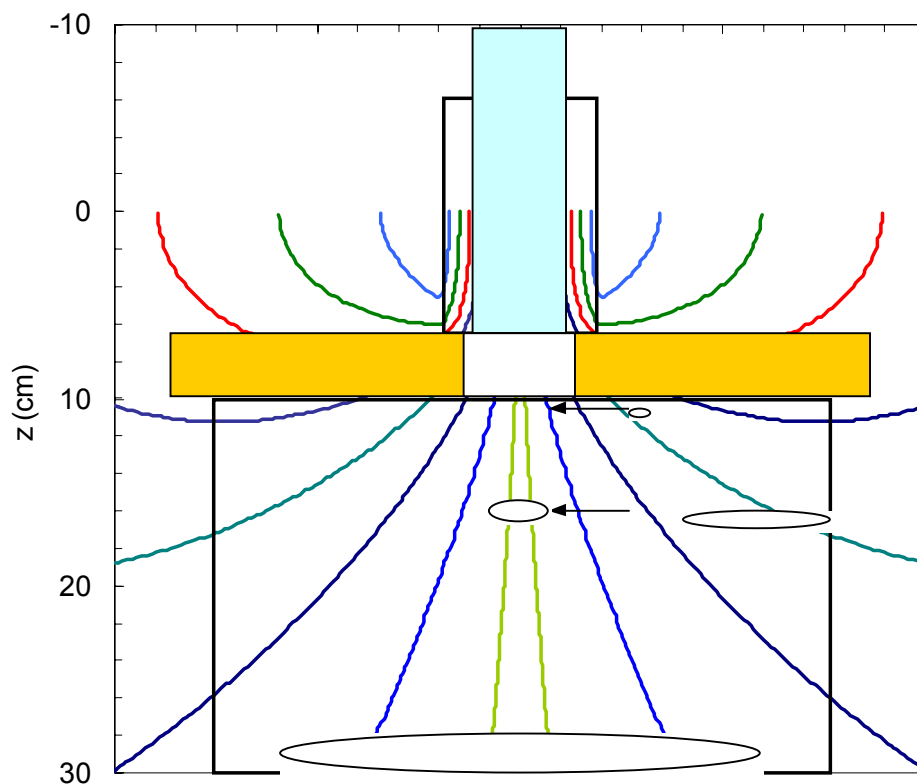


Fig. 4. Schematic of Type 1 test chamber showing magnetic field lines and outlines of the plasma tube, solenoid, entrance flange, and experimental chamber. Probe scans were made at the positions of the arrows. The ellipses show the electron Larmor orbit sizes at various positions when the field in the source is 100 G.

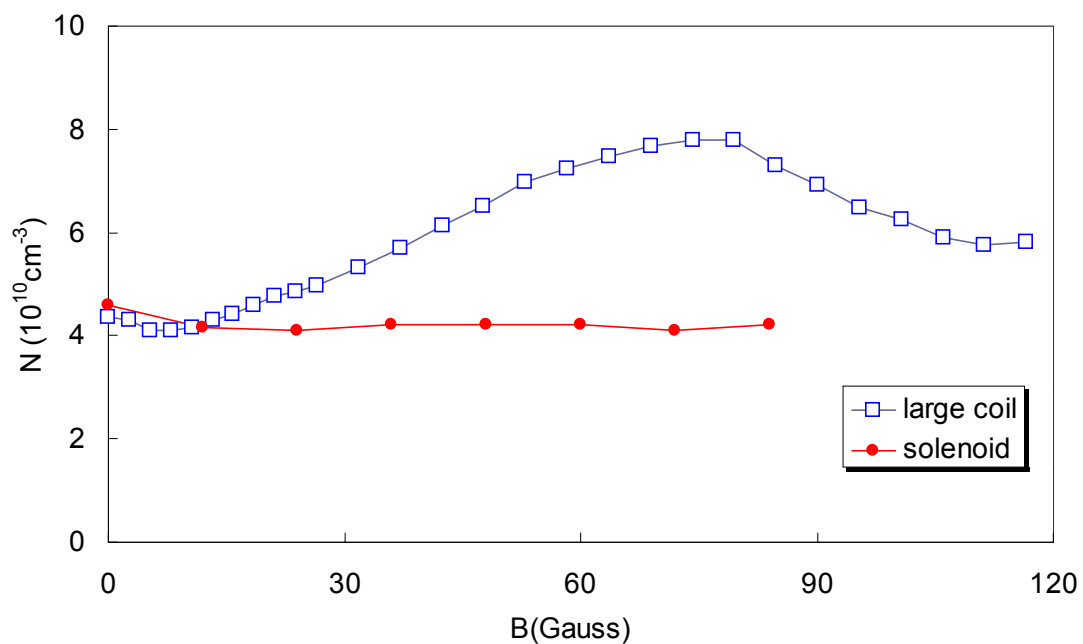


Fig. 5. Comparison of Type 1 and Type 1A sources. 10 mTorr A, 720 W, 13.46 MHz.

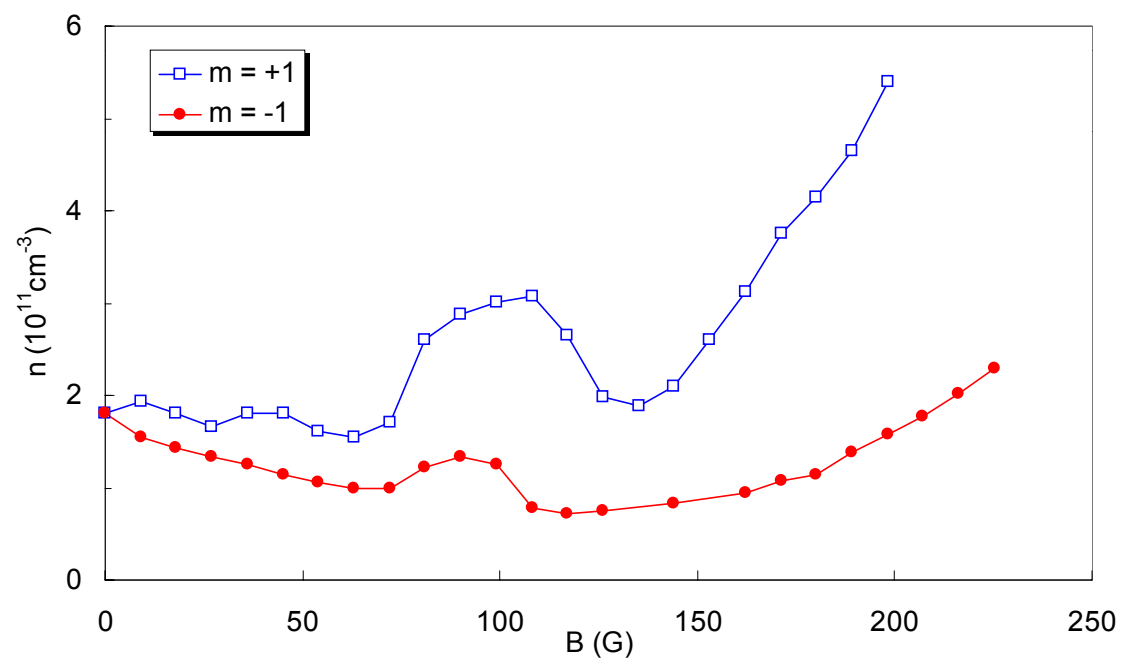


Fig. 6. Low-field density peak with the Type 1A source. 10 mTorr, 1.25 kW, 13.56 MHz, $z = 3$ cm, $r = 5$ cm.

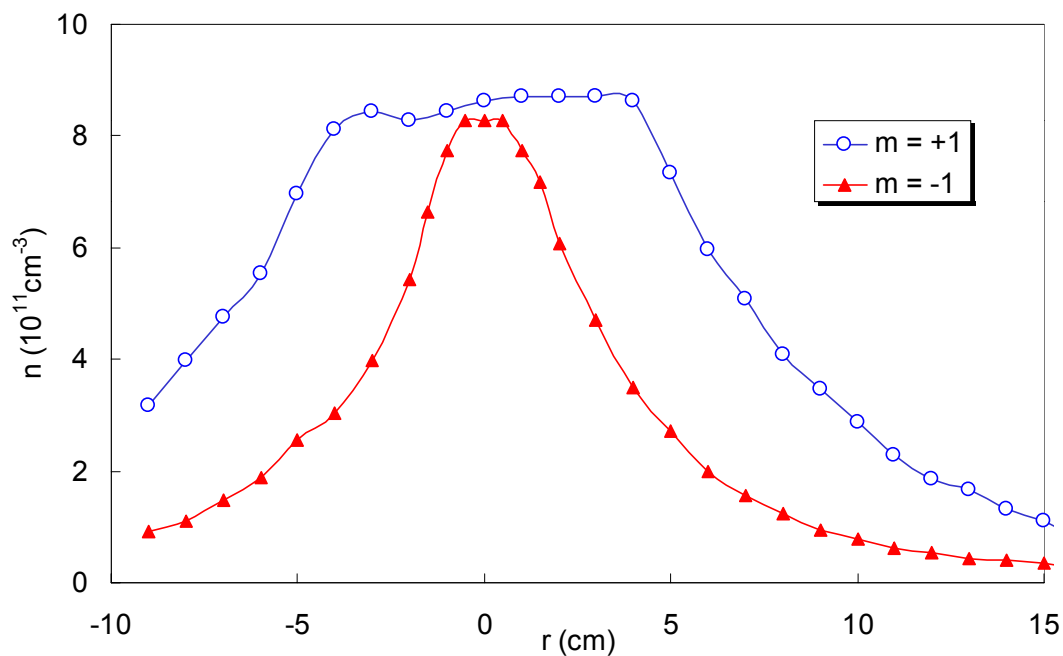


Fig. 7. Density profiles of Type 1A source at $r = 0$ for the $m = +1$ and -1 helicon modes. 150 G, 1 kW, 15 mTorr, 13.56 MHz, $z = 3$ cm.

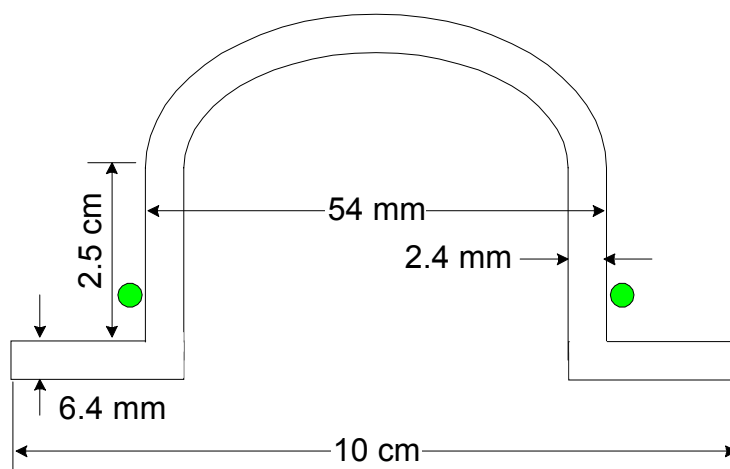


Fig. 8. Schematic of a Type 2 source.

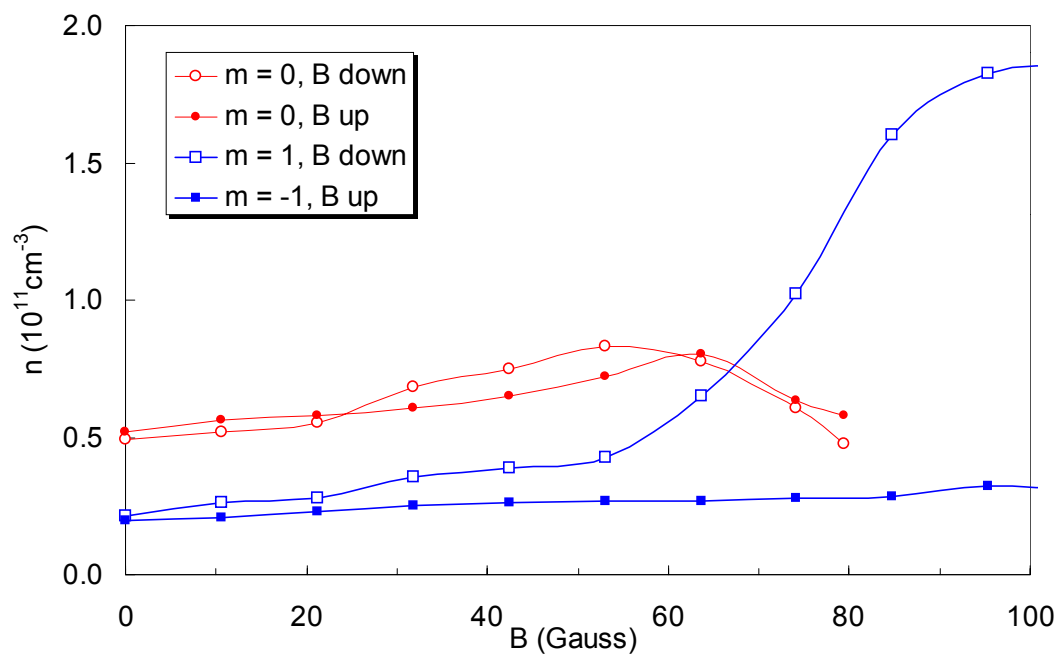


Fig. 9. Density on axis vs magnetic field with $m = \pm 1$ and single-turn $m = 0$ antennas for both directions of B_0 . 435 W, 10 mTorr, 13.56 MHz.

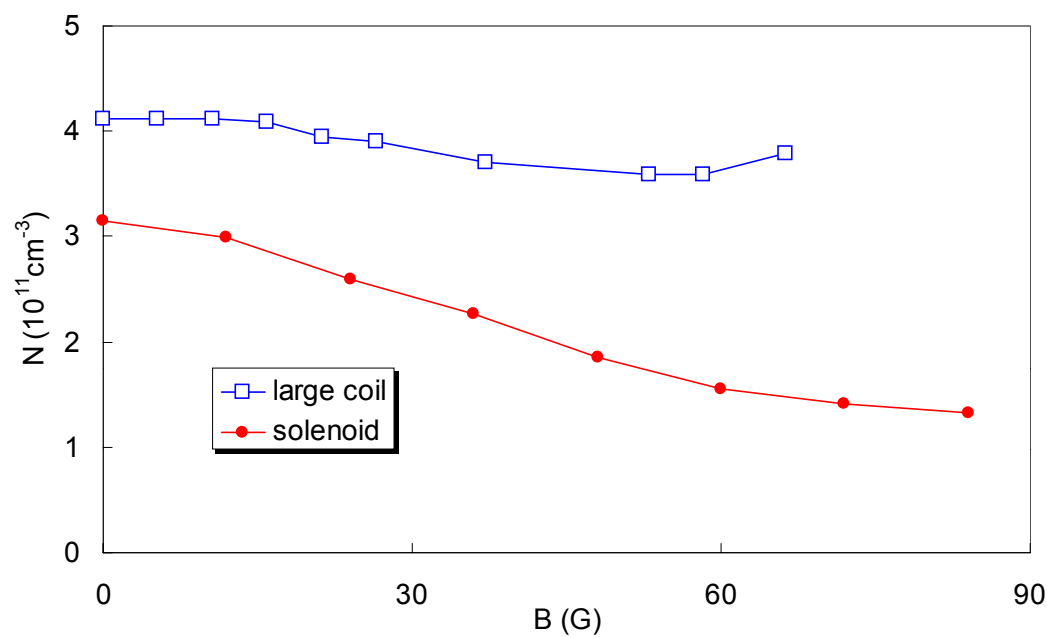


Fig. 10. Density on axis vs B_0 with an $m = 0$ antenna and two types of field coil. The tube length was 7 cm in both cases. 10 mTorr, 720 W, 13.56 MHz, $N = 3$.

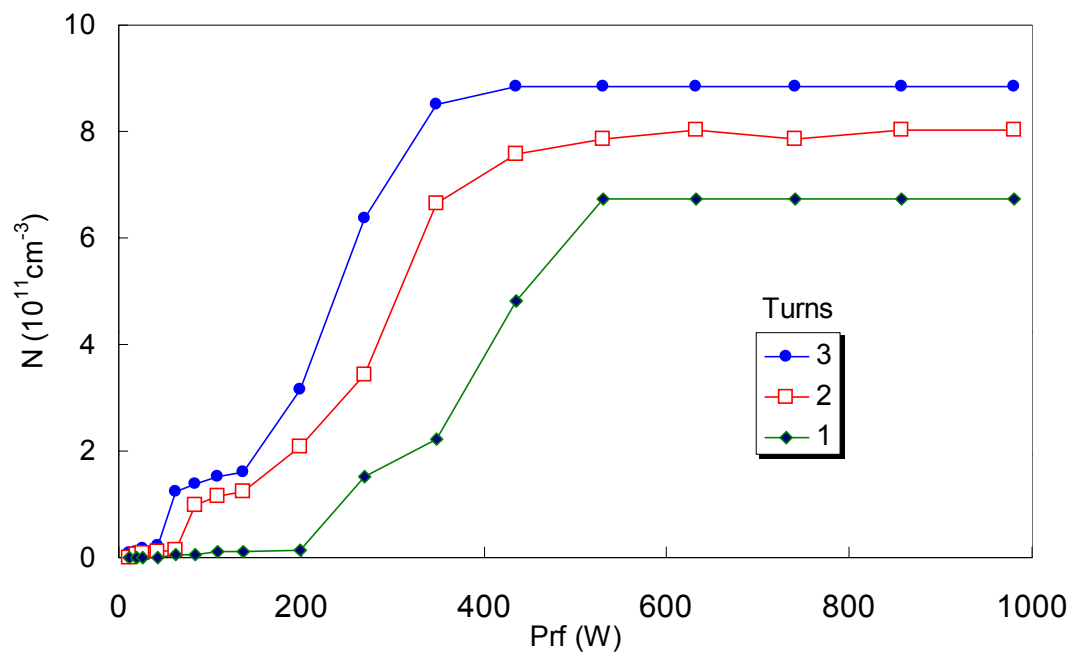


Fig. 11. Dependence of density on the number of turns N in the $m = 0$ antenna. 15 mTorr, 120 G, 13.56 MHz, $z = 3$ cm, $r = 0$.

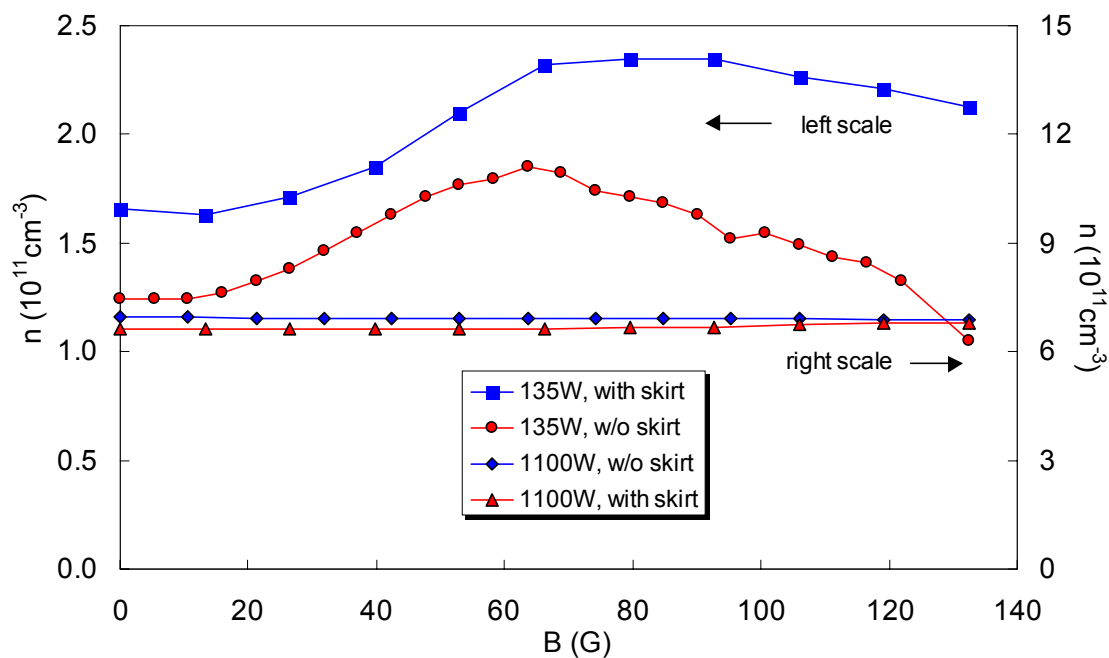


Fig. 12. Effect of an insulating skirt in a Type 2 source at $P_{rf} = 135$ and 1100 W. 10 mTorr, 13.56 MHz, $N = 3$, $z = 3$ cm, $r = 0$.

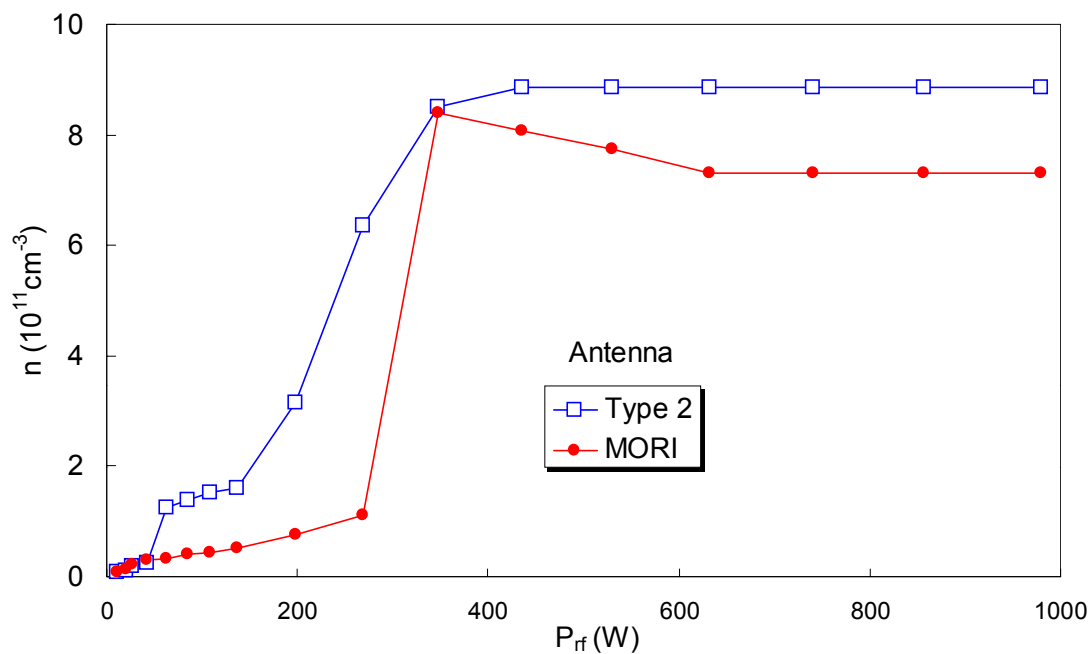


Fig. 13. Density produced by a Type 2 source with $N = 3$, compared with that from a MØRI source with $L = 5$ cm ($\lambda = 10$ cm). 15 mTorr, 120 G, 13.56 MHz, $z = 2$ cm, $r = 0$.

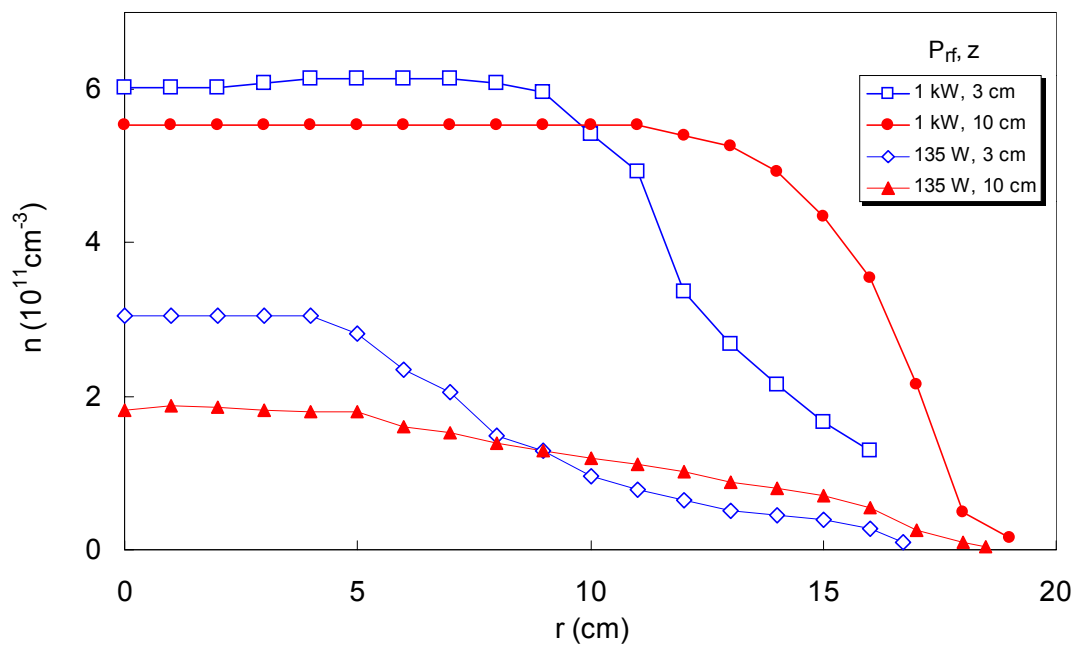


Fig. 14. Density profiles illustrating the diffusion of plasma between $z = 3$ and 10 cm. 20 mTorr, 80 G, 13.56 MHz, $r = 0$.

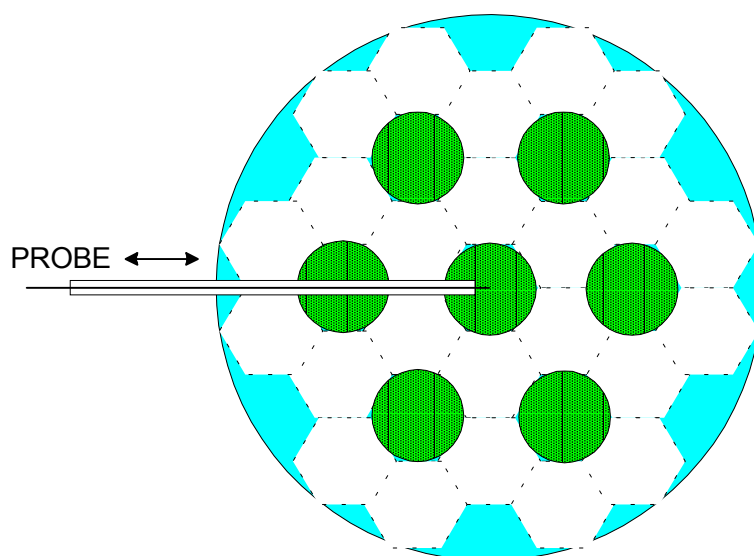


Fig. 15. Arrangement of tubes in a 7-tube distributed source.

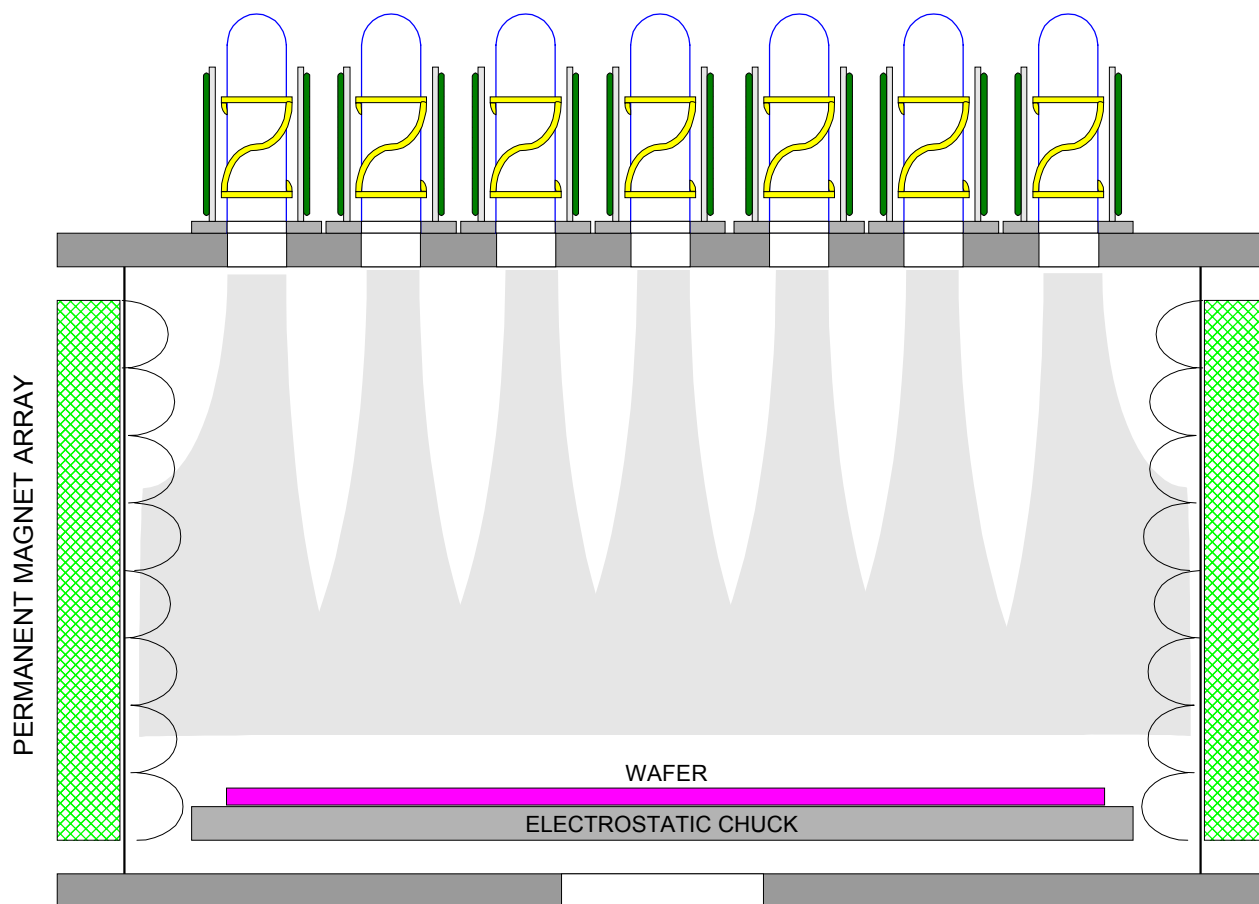


Fig. 16. Schematic of a 7-tube source with a magnetic bucket. The Type 1 tubes are arranged as in Fig. 15 (not in line, as depicted here).

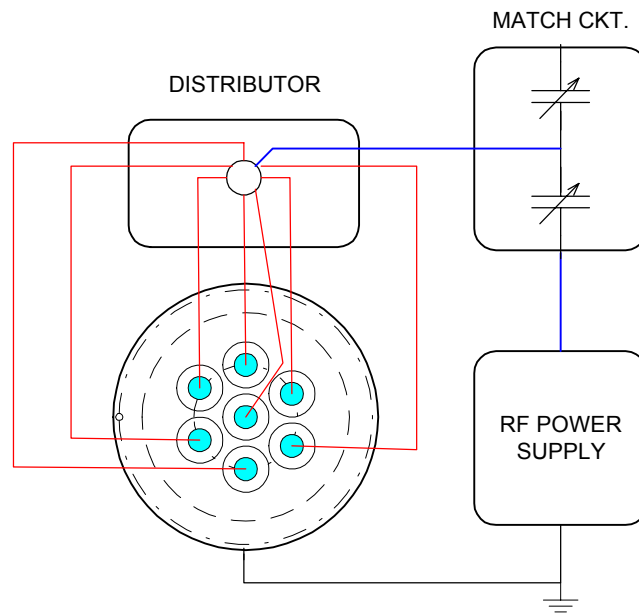
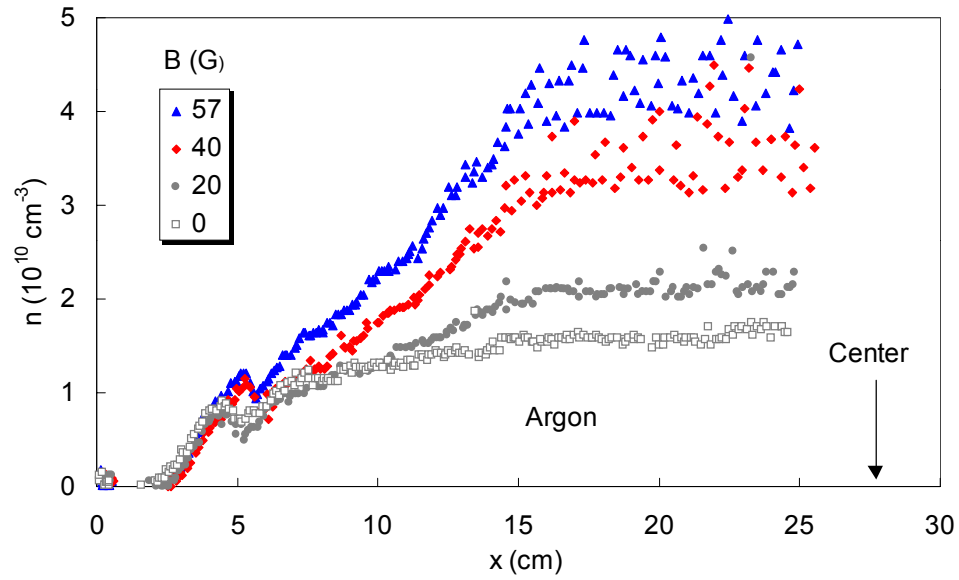
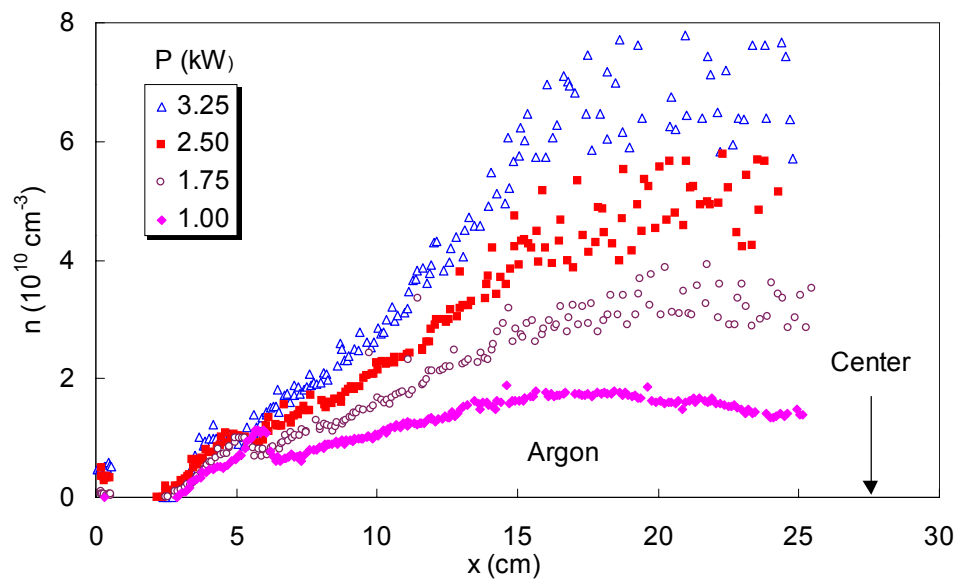


Fig. 17. Schematic of the matching and distribution circuit.

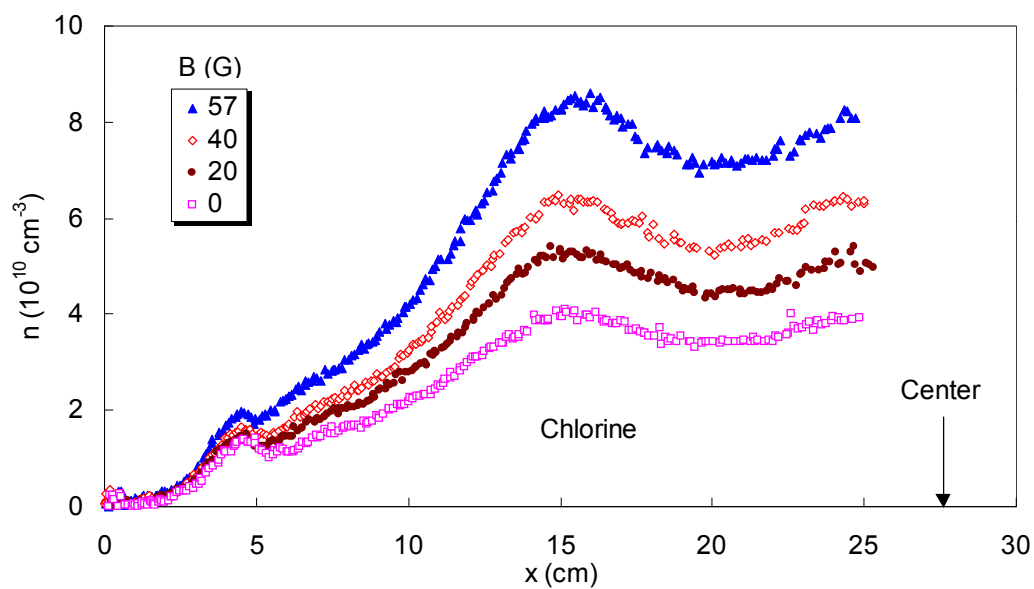


(a)

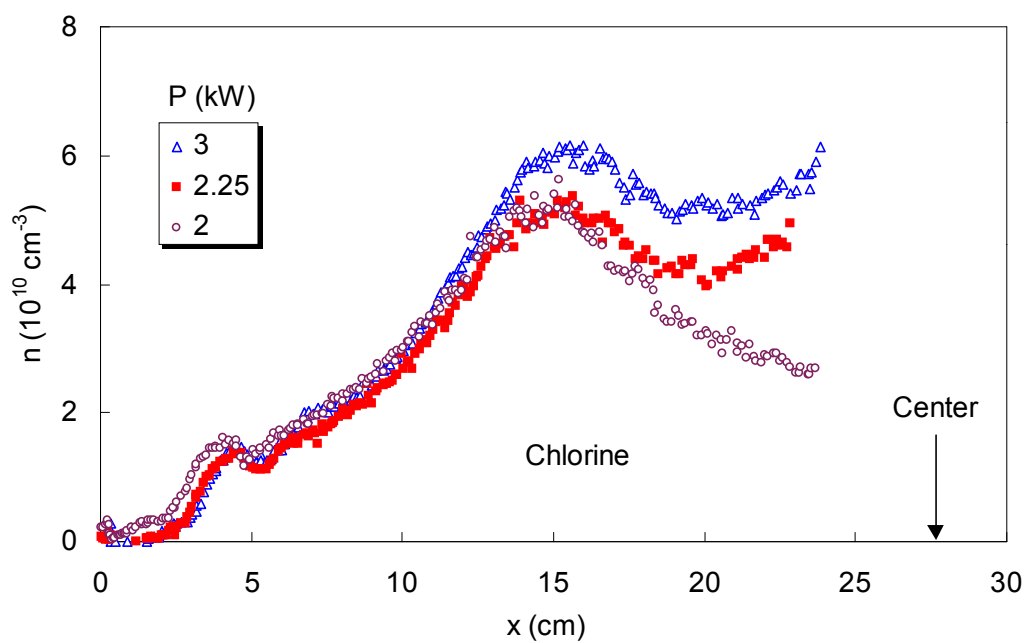


(b)

Fig. 18. Density profiles along one radius of a 7-tube array of Type 1 sources vs (a) magnetic field at $P_{\text{rf}} = 1.75$ kW, and (b) RF power at $B_0 = 30$ G, 18 mTorr A, 13.56 MHz, $z = 9$ cm.



(a)



(b)

Fig. 19. Density profiles along one radius of a 7-tube array of Type 1 sources vs (a) magnetic field at $P_{\text{rf}} = 3$ kW, and (b) RF power at $B_0 = 30$ G, 10 mTorr Cl, 13.56 MHz, $z = 9$ cm.

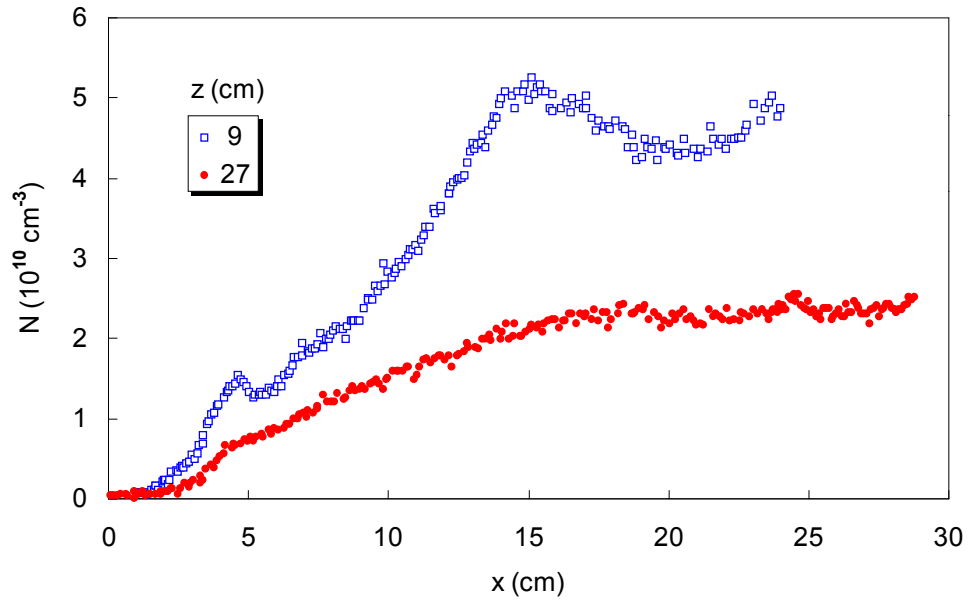


Fig. 20. Diffusion of plasma in a Type 1 array source between $z = 9$ and 27 cm. 10 mTorr Cl, 2.5 kW, 13.56 MHz, 30 G.

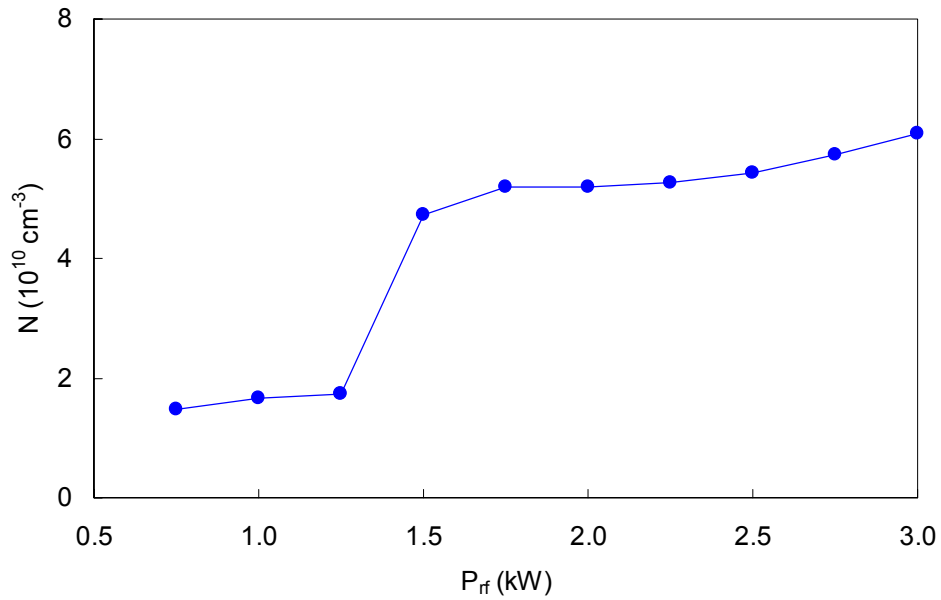


Fig. 21. Jump transition in a Type 1 array as P_{rf} is increased. 10 mTorr Cl, 30 G, 13.56 MHz, $r = 0$.

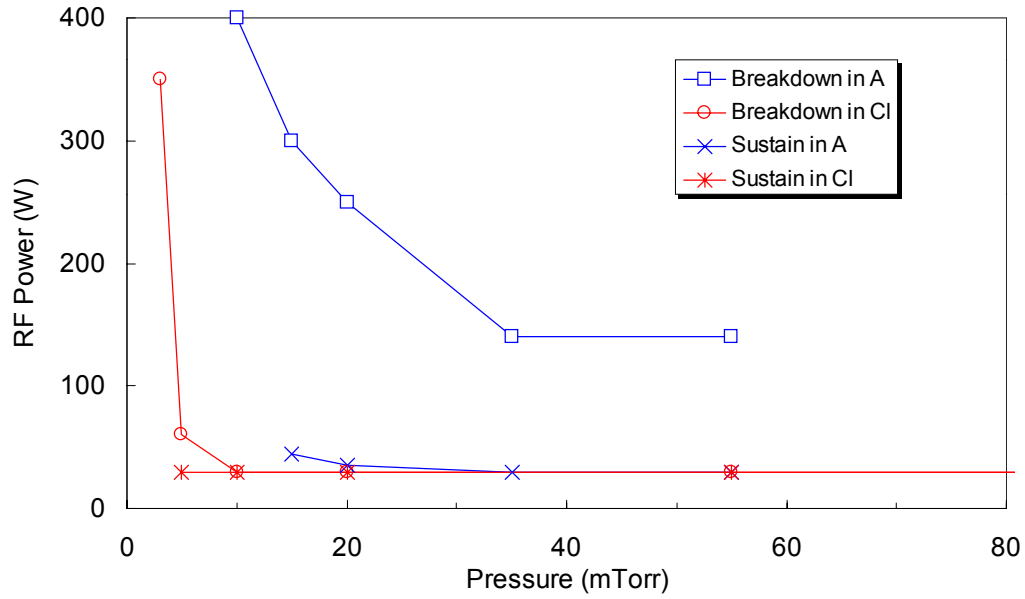


Fig. 22. RF power required to break down and sustain A and Cl discharges in a Type 1 array, as a function of p_0 at $B_0 = 0$

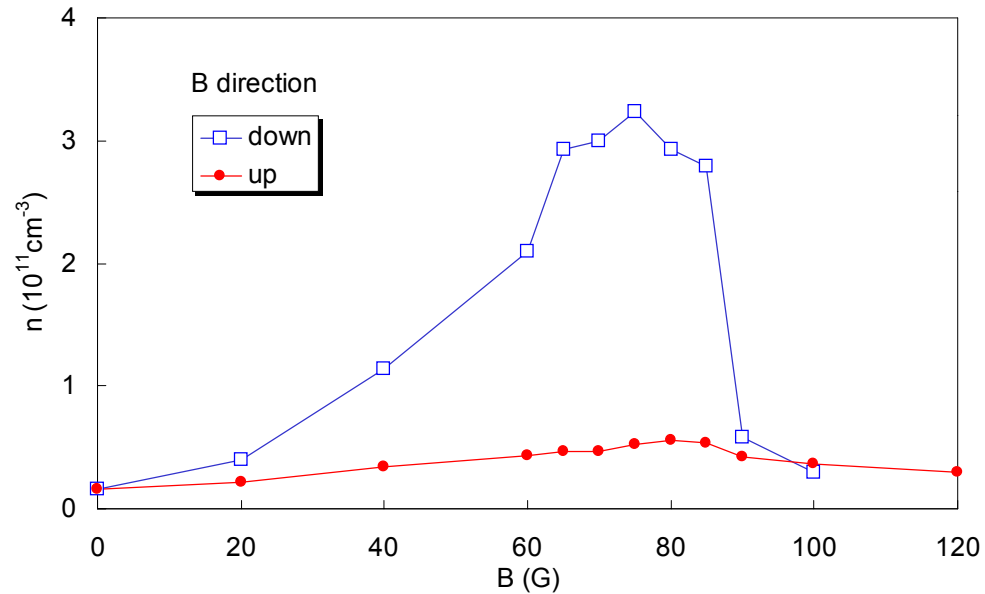


Fig. 23. The low-field density peak in a Type 1 array source appearing strongly when the direction of B_0 corresponds to the excitation of the $m = +1$ helicon mode. 4 mTorr Cl, 3.3 kW, $z = 20$ cm, $r = 5$ cm.

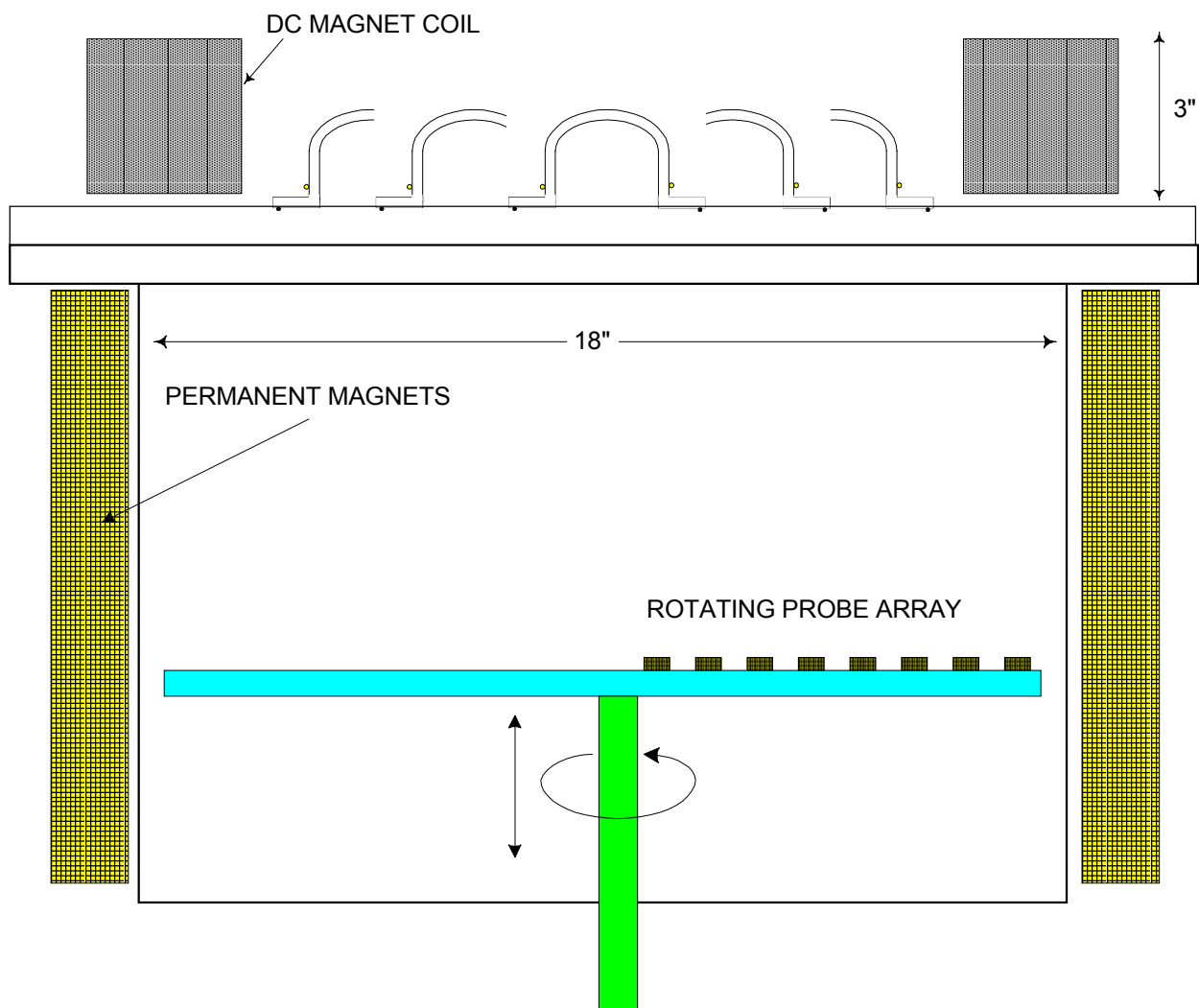


Fig. 24. Schematic of a Type 2 array source with large magnet coil. Also shown is the "Lazy Susan" rotatable ion collector array.

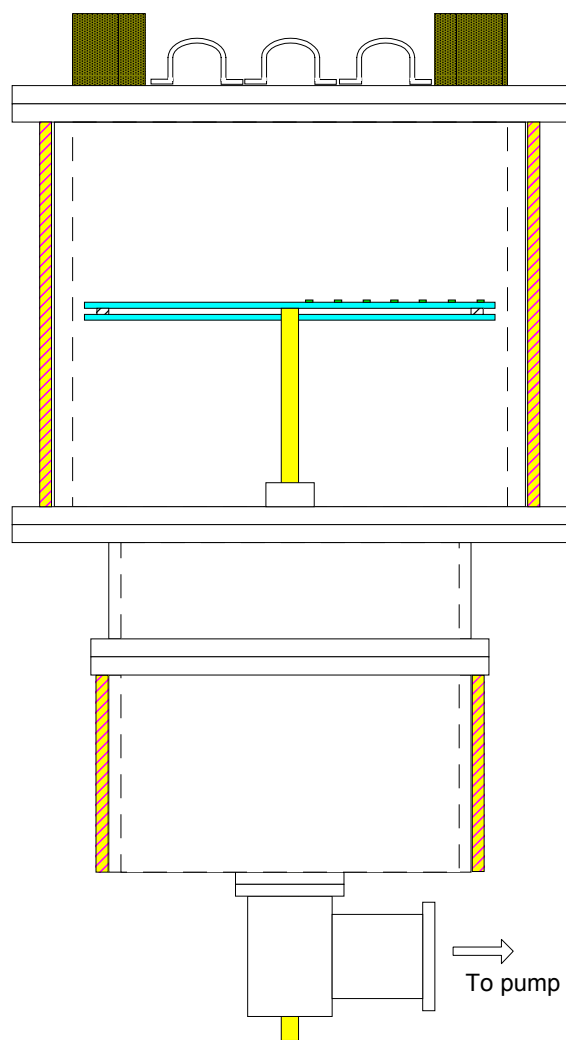


Fig. 25. Experimental setup with magnet buckets of two diameters.

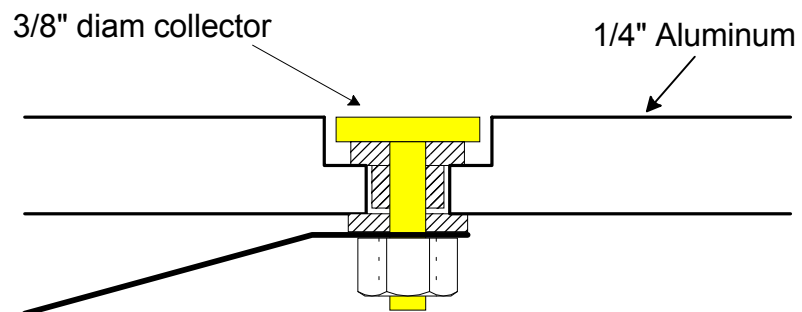


Fig. 26. Schematic of an ion collector in the rotatable probe array.

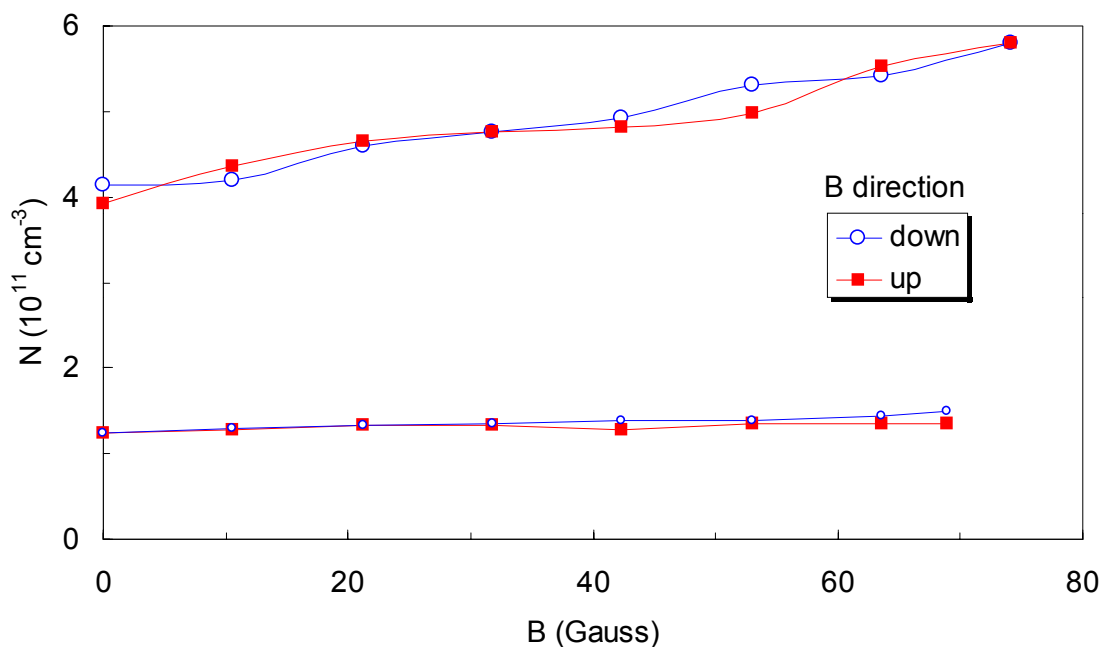


Fig. 27. Density vs B_0 in $m = 0$ array sources, showing insensitivity to field direction. Top: a single Type 2 tube with $N = 1$, $z = 10$ cm, $r = 5$ cm. Bottom: a 7-tube Type 1A array with $N = 5$. 10 mTorr, 1.4 kW, 13.56 MHz.

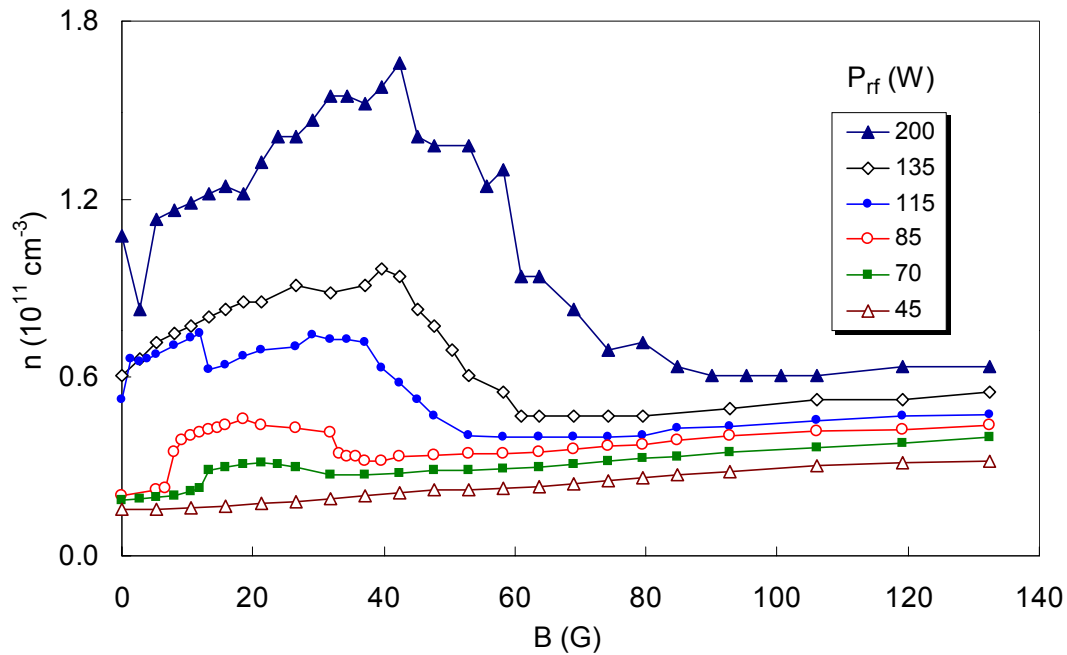


Fig. 28. The low-field density peak at intermediate powers in a Type 2 array. 8 mTorr, 13.56 MHz, $N = 5$.

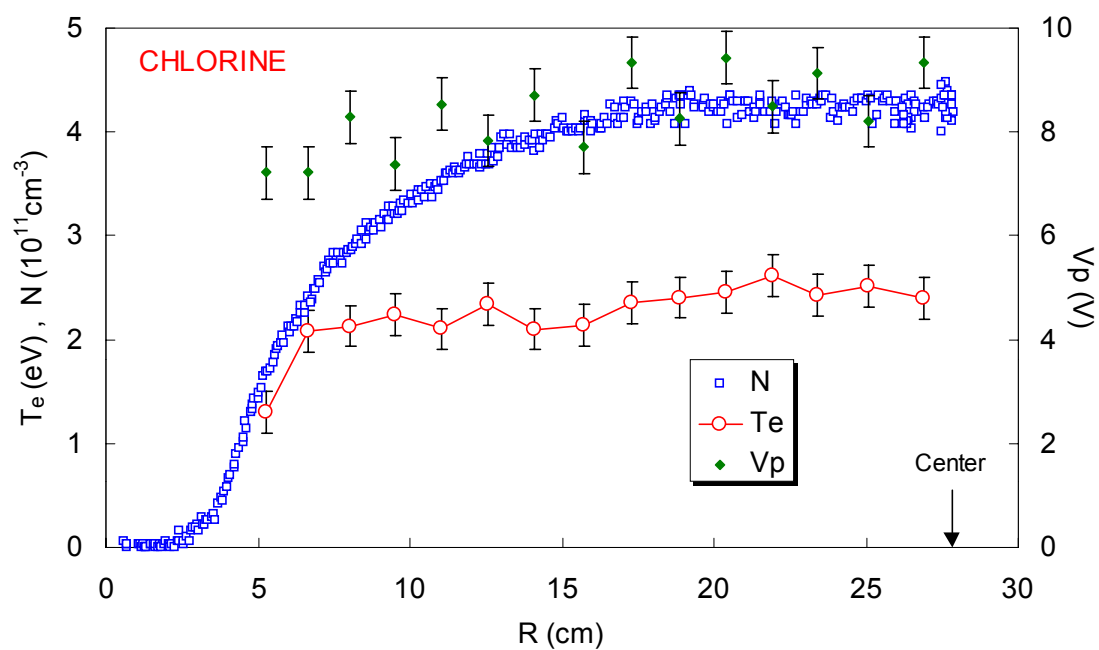
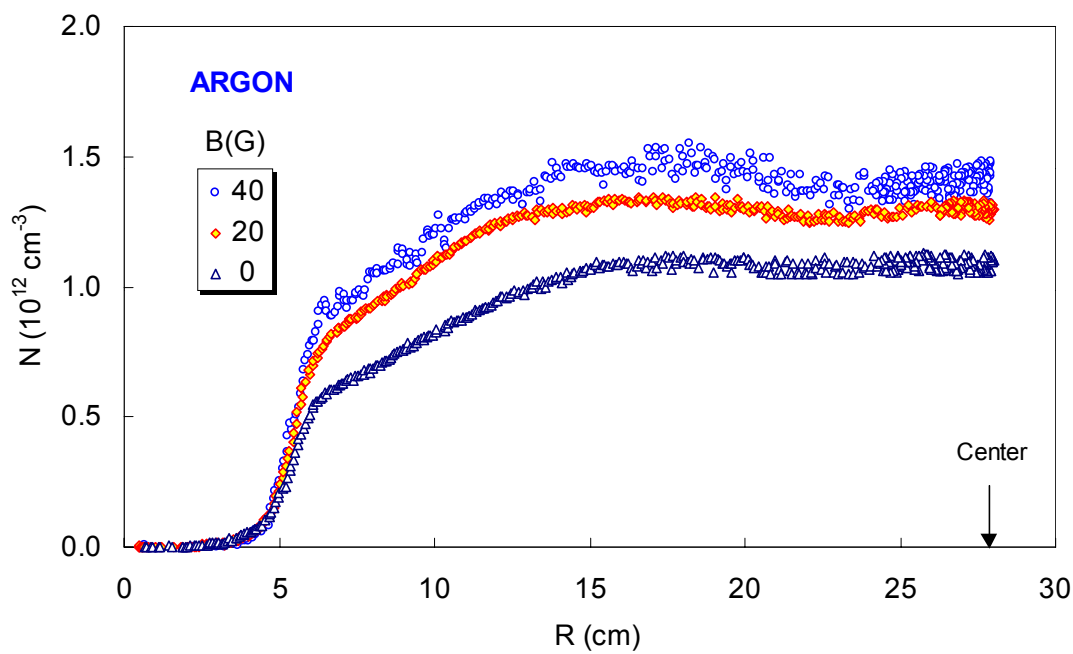
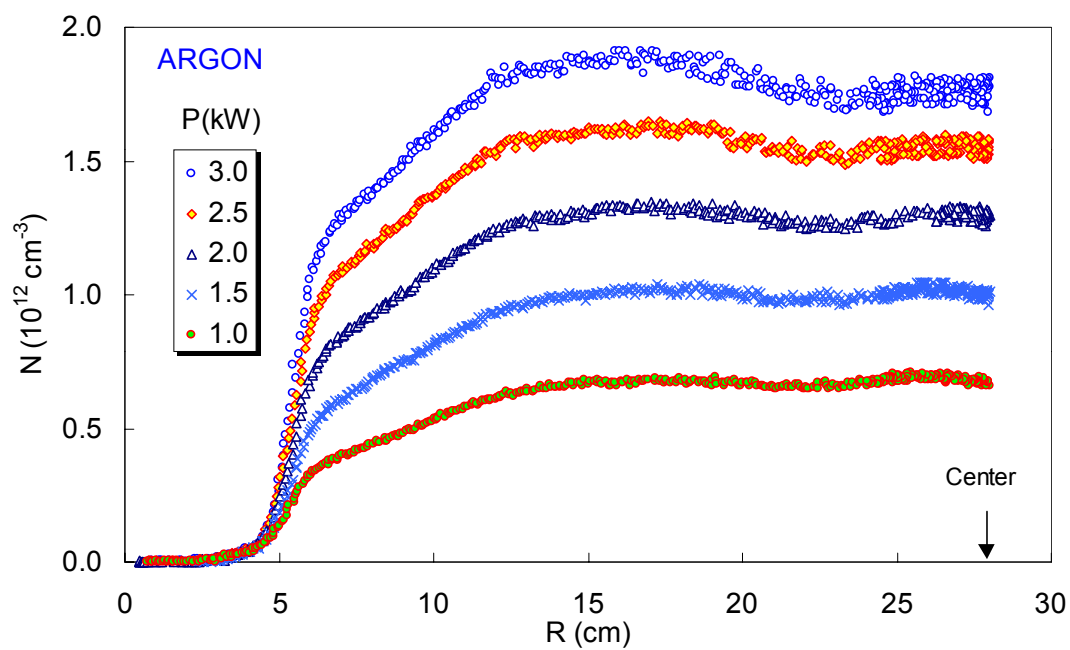


Fig. 29. Radial profiles of n , T_e , and V_p in a Type 2 source. R is the radial distance from the wall. V_p is given on the right-hand scale. 3 mTorr Cl, 35 G, 3 kW, 13.56 MHz, $z = 27$ cm.

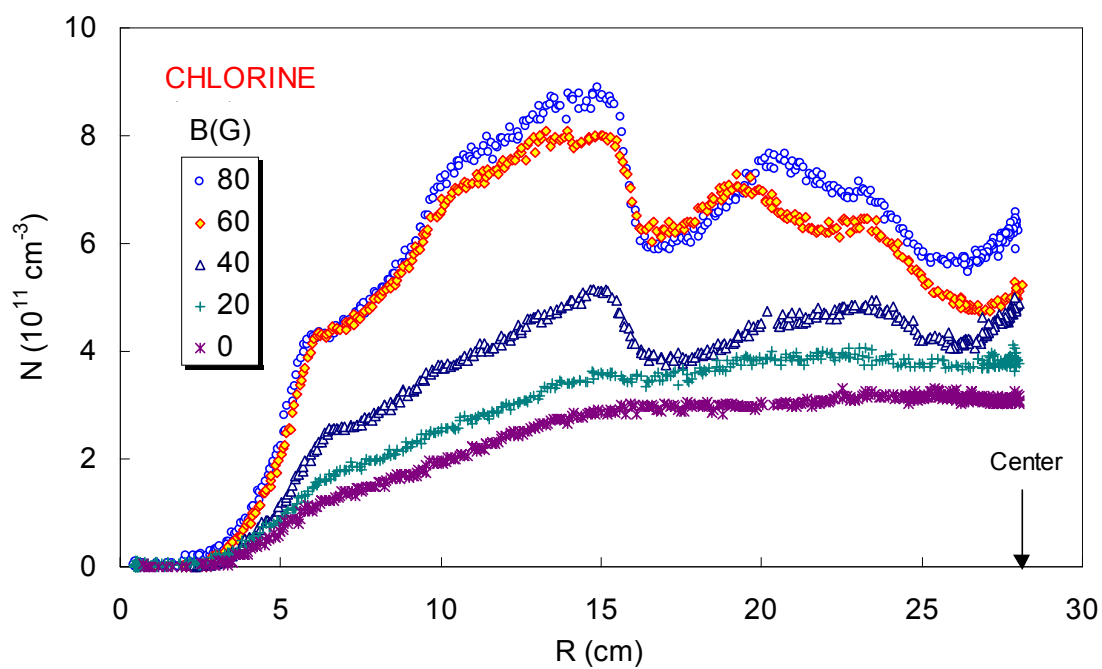


(a)

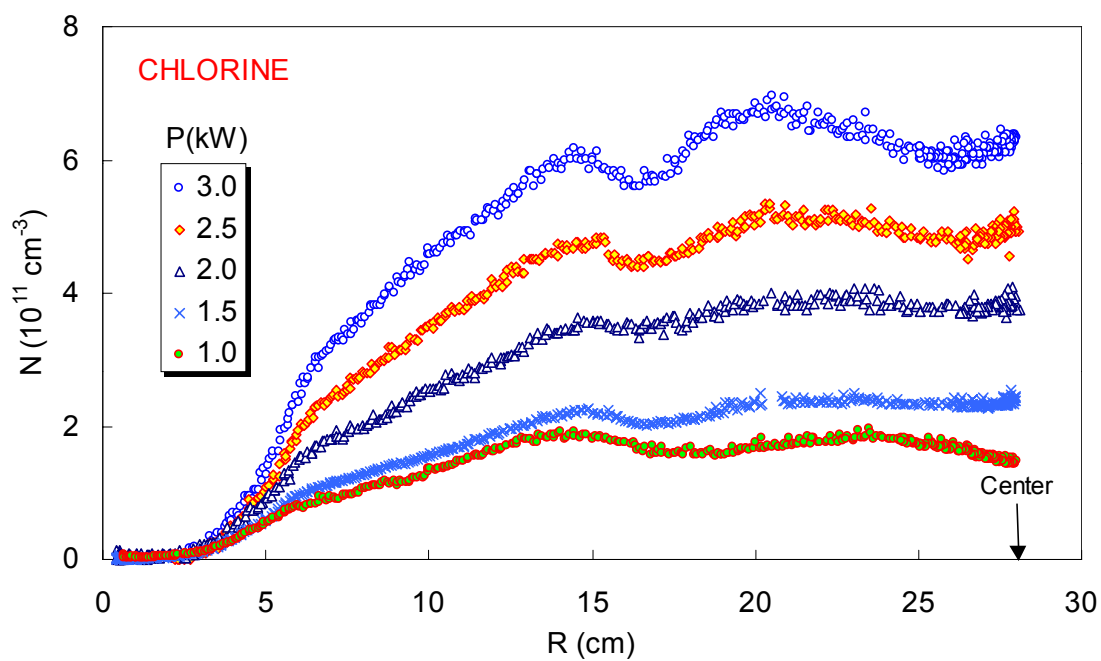


(b)

Fig. 30 Radial density profiles in argon in a Type 2 source, as functions of (a) B_0 and (b) P_{rf} .
5 mT, 20 G, 2 kW, 13.56 MHz, $N = 2$, $z = 7$ cm unless otherwise noted.

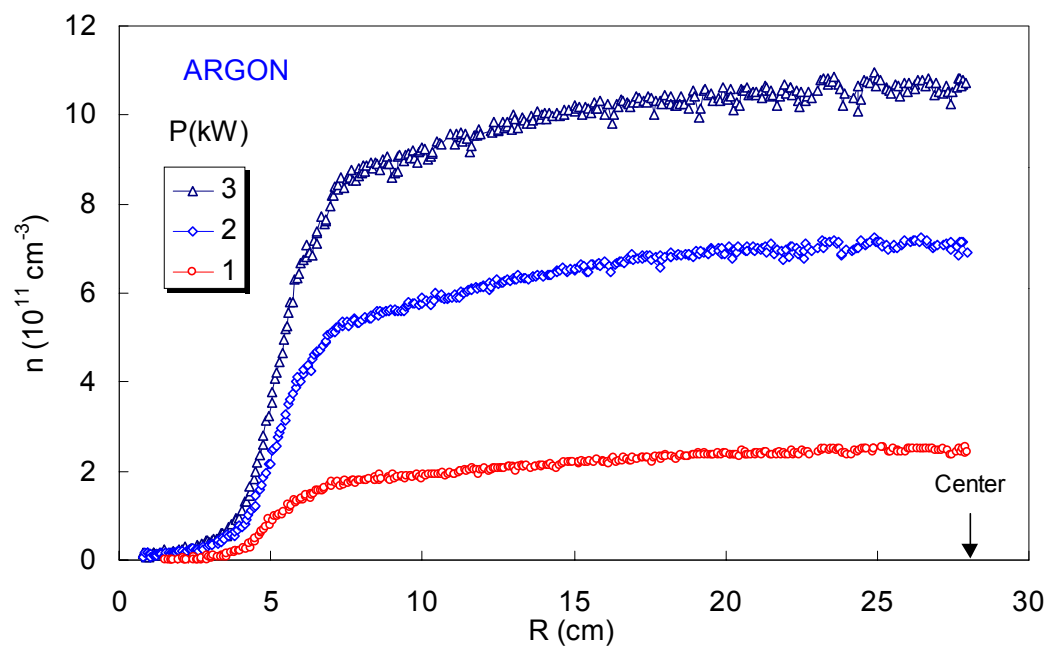


(a)

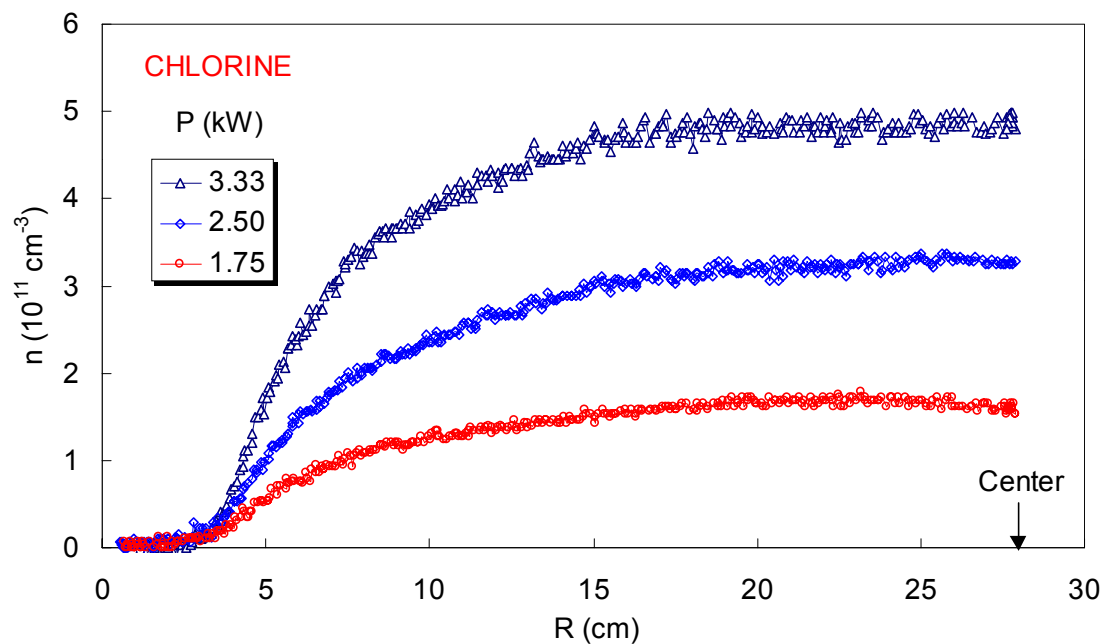


(b)

Fig. 31. Radial density profiles in chlorine in a Type 2 source, as functions of (a) B_0 and (b) P_{rf} . 3 mT, 20 G, 2 kW, 13.56 MHz, $N = 2$, $z = 7$ cm unless otherwise noted.



(a)



(b)

Fig. 32. Downstream radial density profiles in (a) 5 mTorr A at 20 G and (b) 3 mTorr Cl at 35 G in a Type 2 source. $f=13.56$ MHz, $N=2$, $z = 27$ cm.

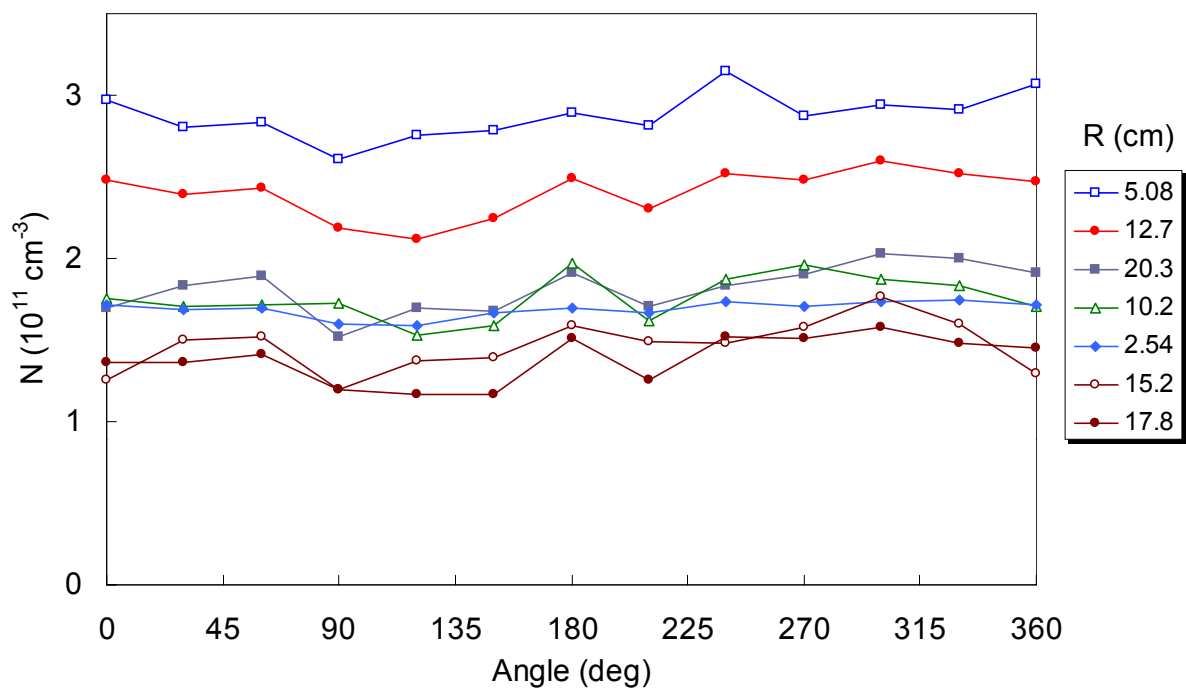


Fig. 33. Raw data from the Lazy Susan probe. 3 mTorr Cl, 20 G, 2 kW, 13.56 MHz, $N=2$, $z = 30$ cm.

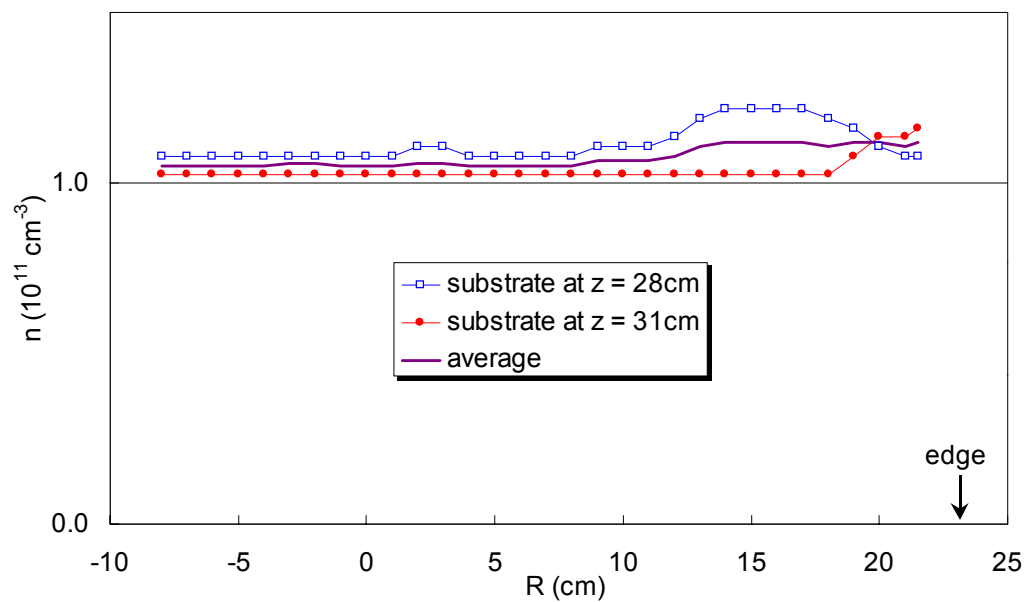


Fig. 34. Radial density profile with Langmuir probe at $z = 27.5$ cm and Lazy Susan probe at $z = 28$ and 31 cm. 2 mTorr, 60 G, 1.4 kW, 13.56 MHz, $N = 4$.

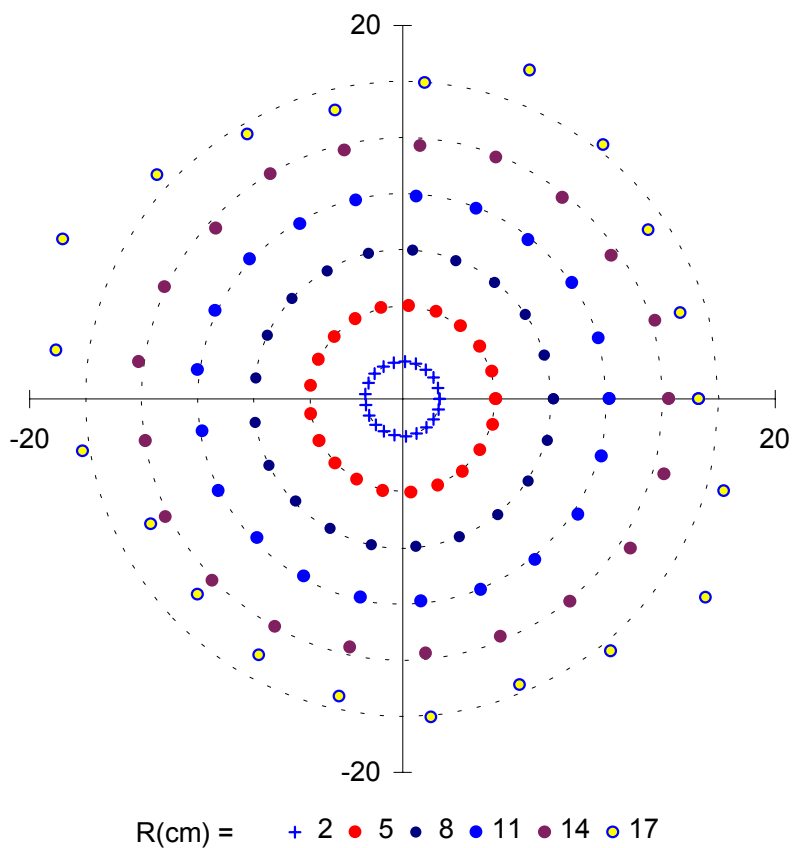


Fig. 35. Azimuthal density uniformity at various radii in a 20×20 cm cross section at $z = 30$ cm. The density at each radius is plotted relative to the dashed circle at that radius. 2 mTorr A, 40 G, 1.4 kW, $N = 4$.

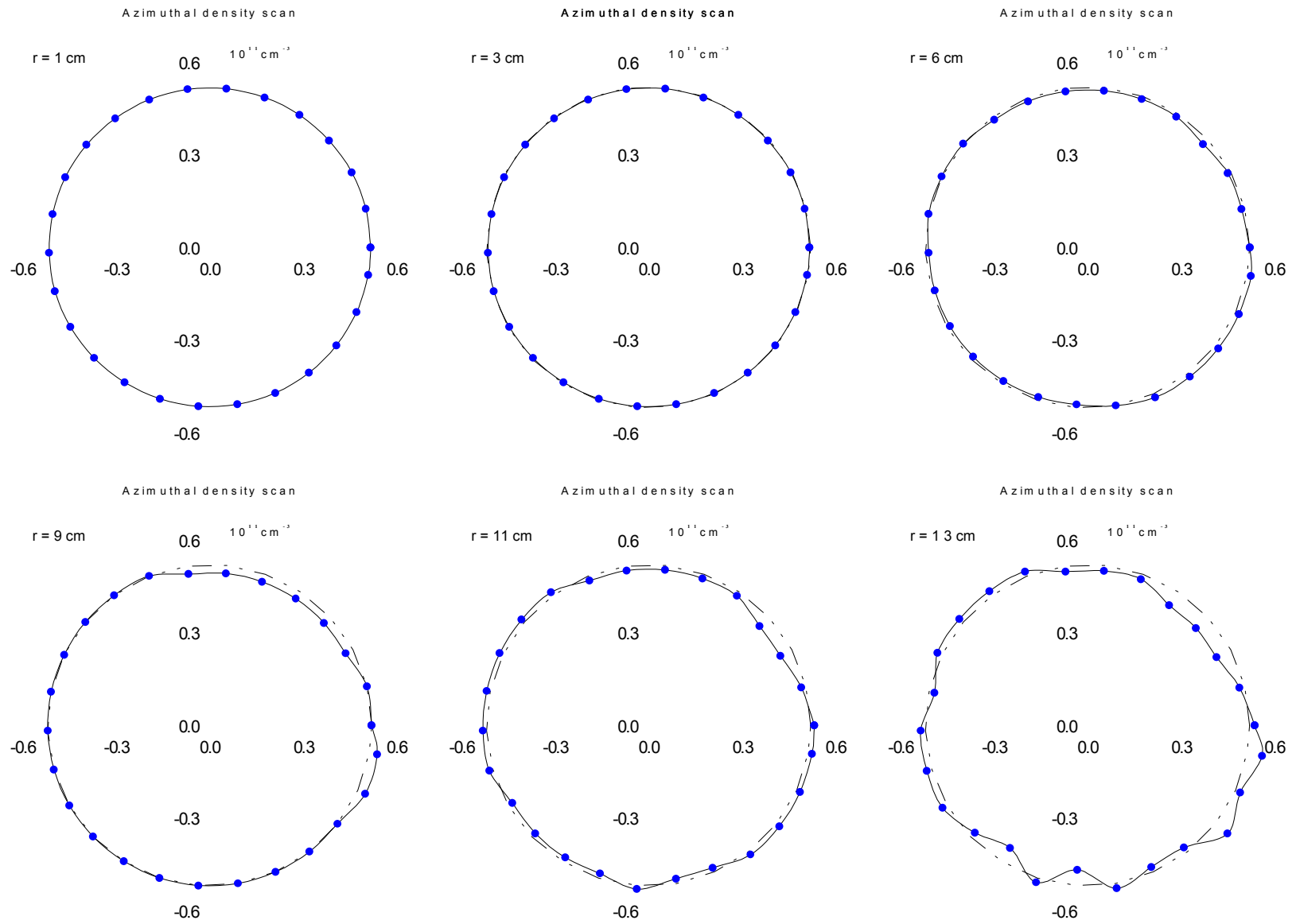


Fig. 36. Polar plots of $n(\theta)$ with increasing radius in units of 10^{11} cm^{-3} . 20 mTorr A, 75 G, 1.3 kW, 13.56 MHz, $z = 20$ cm.

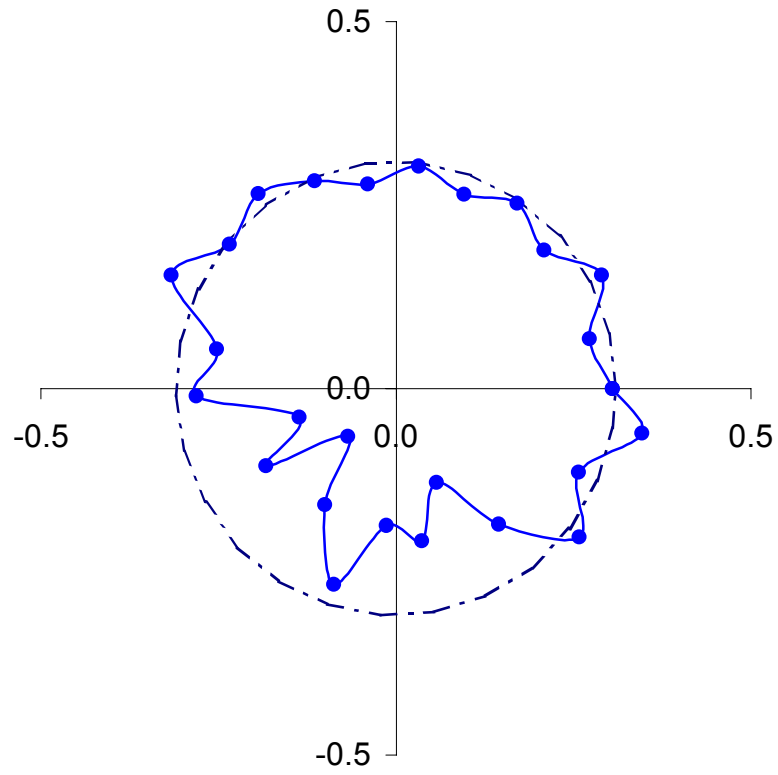


Fig. 37. Azimuthal density scan at $r = 15$ cm, about 1.5 cm from permanent magnet array on wall.

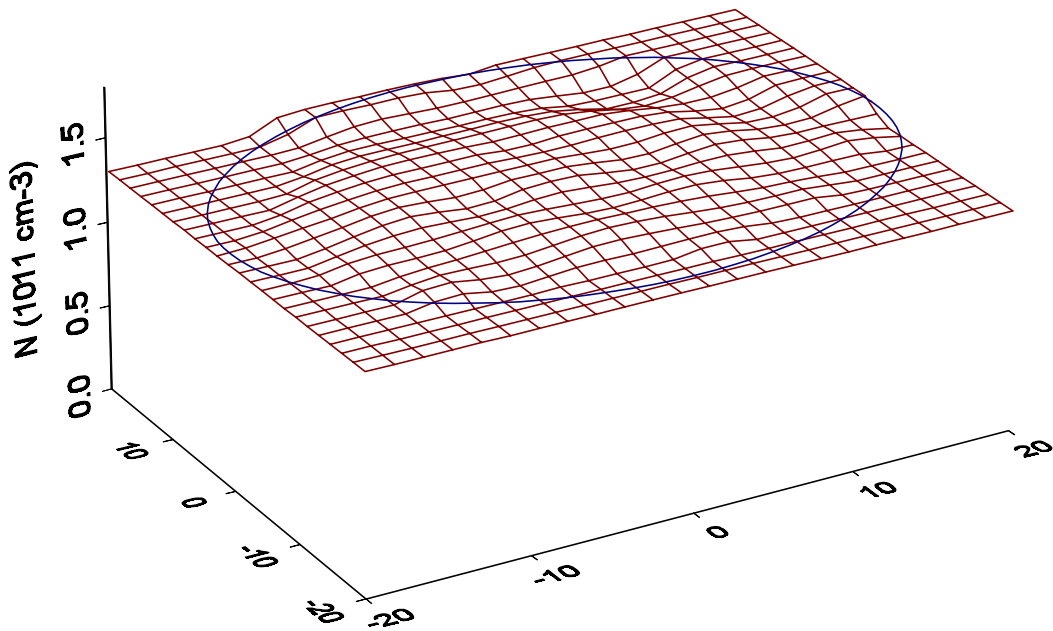


Fig. 38. 3D plot of the data of Fig. 36.

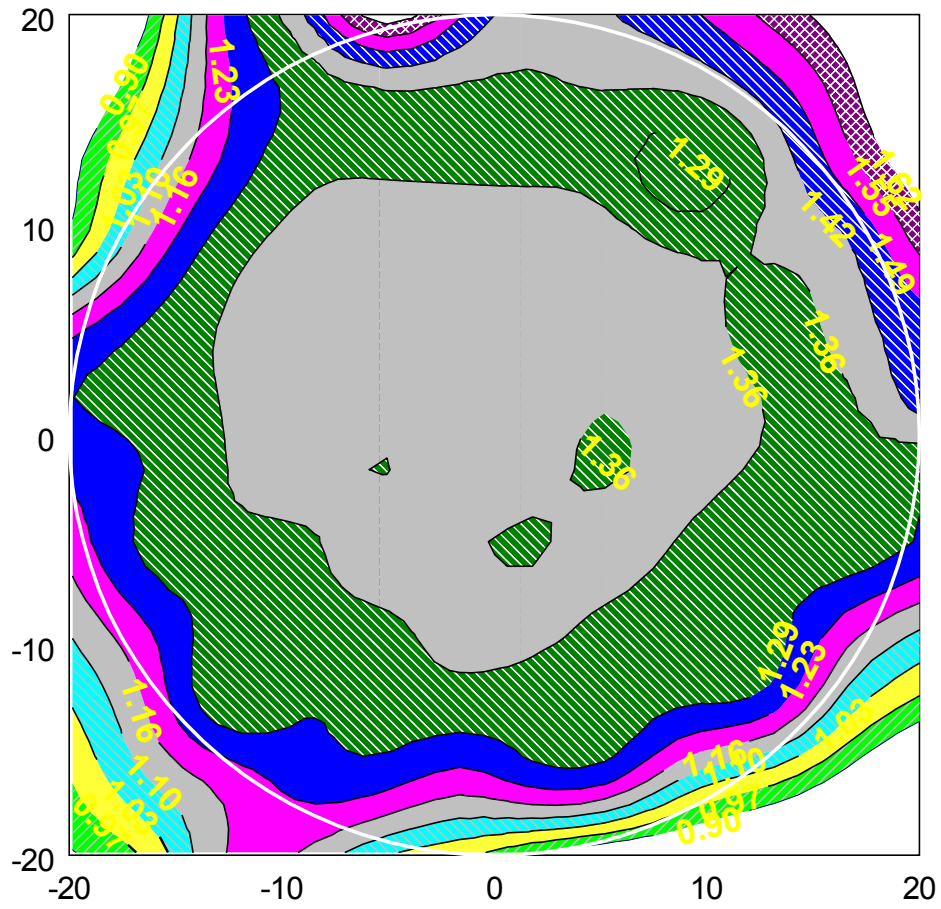


Fig.39. Density contour plot of the data of Fig. 36. The contour interval is $\approx 4\%$. Only the data inside the 40-cm diameter circle is meaningful.

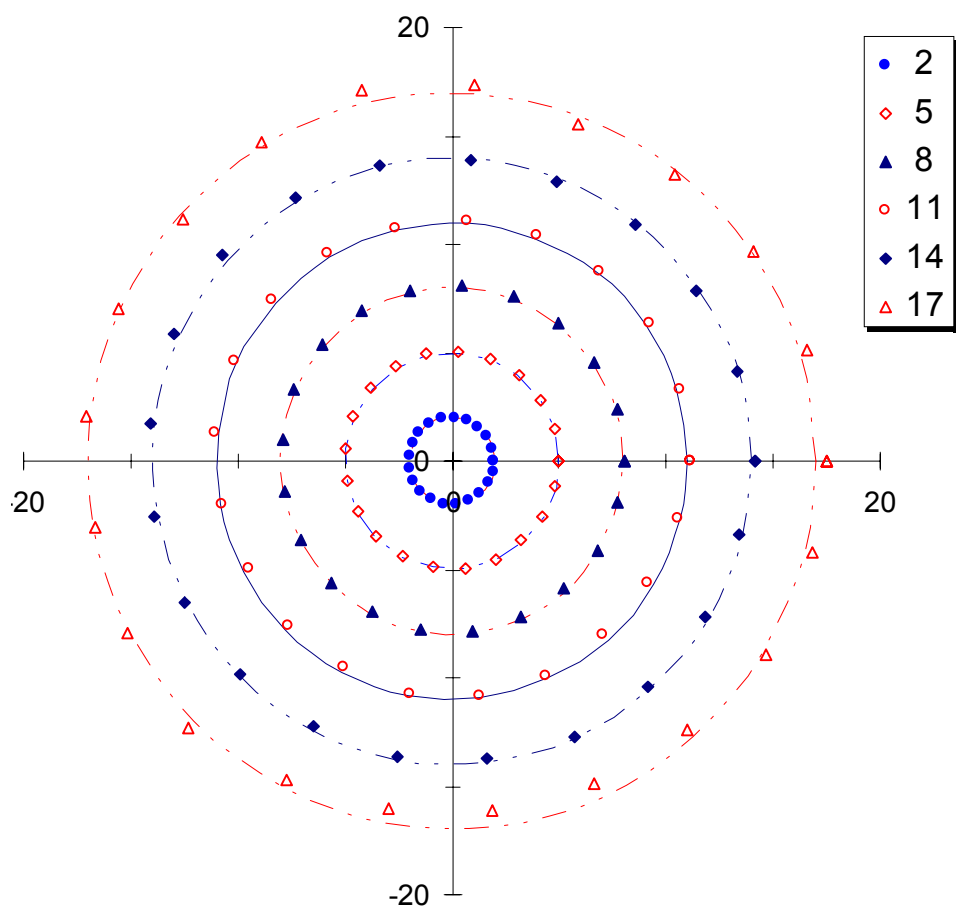


Fig.40. Polar plot of density at various radii (cm) with two independently adjustable power supplies. 15 mTorr A, 100 G, 1.6 kW, 27.12 MHz, $N = 2$.

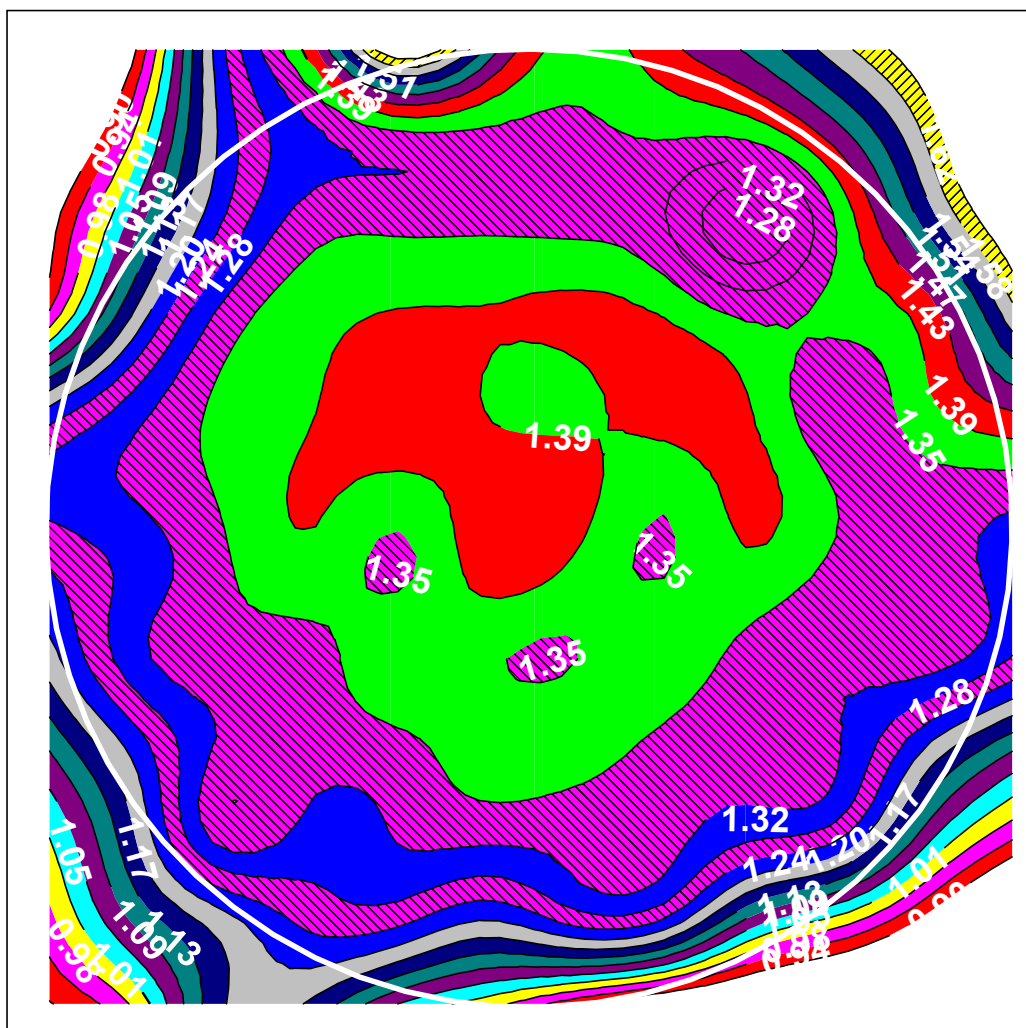


Fig. 41. Contour plot of the data of Fig. 40. The contour interval is 3%. Only the data inside the 40-cm diameter circle is meaningful.